Arctic Sea Ice Characterization Using Spaceborne Fully Polarimetric L-, C-, and X-Band SAR With Validation by Airborne Measurements

Suman Singha, *Member, IEEE*, Malin Johansson, *Member, IEEE*, Nicholas Hughes, *Member, IEEE*, Sine Munk Hvidegaard, and Henriette Skourup

Abstract— In recent years, spaceborne synthetic aperture radar (SAR) polarimetry has become a valuable tool for sea ice analysis. Here, we employ an automatic sea ice classification algorithm on two sets of spatially and temporally near coincident fully polarimetric acquisitions from the ALOS-2, Radarsat-2, and TerraSAR-X/TanDEM-X satellites. Overlapping coincident sea ice freeboard measurements from airborne laser scanner data are used to validate the classification results. The automated sea ice classification algorithm consists of two steps. In the first step, we perform a polarimetric feature extraction procedure. Next, the resulting feature vectors are ingested into a trained neural network classifier to arrive at a pixelwise supervised classification. Coherency matrix-based features that require an eigendecomposition are found to be either of low relevance or redundant to other covariance matrix-based features, which makes coherency matrix-based features dispensable for the purpose of sea ice classification. Among the most useful features for classification are matrix invariant-based features (geometric intensity, scattering diversity, and surface scattering fraction). Classification results show that 100% of the open water is separated from the surrounding sea ice and that the sea ice classes have at least 96.9% accuracy. This analysis reveals analogous results for both X-band and C-band frequencies and slightly different for the L-band. The subsequent classification produces similarly promising results for all four acquisitions. In particular, the overlapping image portions exhibit a reasonable congruence of detected sea ice when compared with high-resolution airborne measurements.

S. Singha is with the Maritime Safety and Security Lab, Remote Sensing Technology Institute, German Aerospace Center, 28199 Bremen, Germany (e-mail: suman.singha@dlr.de).

M. Johansson is with the Department of Physics and Technology, The Arctic University of Norway, 9037 Tromsø, Norway.

N. Hughes is with the Norwegian Ice Service, Norwegian Meteorological Institute, 9293 Tromsø, Norway.

S. M. Hvidegaard and H. Skourup are with the National Space Institute, Technical University of Denmark, 2800 Kongens Lyngby, Denmark.

I. INTRODUCTION

OVER more than three decades, synthetic aperture radar (SAR) has become an invaluable asset for the monitoring of Arctic and Antarctic regions. In contrast to optical imaging, SAR is not impeded by cloud coverage, fog, or the lack of daylight. Given that sea ice coverage is often in remote regions that are otherwise hard to reach, polar-orbiting satellites with global coverage are ideal for any type of monitoring purpose. Spaceborne SAR sensors can cover almost any region on the globe with short revisit times. Additionally, the polar regions above 75°N and below 75°S are covered multiple times each day enabling high temporal resolution studies of, e.g., sea ice drift and sea ice concentration. Furthermore, different SAR missions utilize different frequencies and these can provide complementary information due to their different sea ice penetration depths. Satellites, such as RADARSAT-1 and 2, ERS-1 and 2, ENVISAT in the C-band, and TerraSAR-X (TS-X) in the X-band, have proven the suitability of SAR sensors for investigating sea ice in Arctic and Antarctic regions. Moreover, L-band SAR is less sensitive to the onset of melting, therefore, provide complementary information in the early melt season [1], [2]. Due to this unique complementary information and the increased penetration depth compared to C- and X-band, L-band SAR provide a better separability between first year ice (FYI) and multiyear ice (MYI) during the melt season [3]. In this paper, we investigate the accuracy of an automatic sea ice classification algorithm for different SAR frequencies (L-, C-, and X-bands) and validate it with high-resolution laser scanner data.

Medium spatial resolution SAR images extend up to a few hundred kilometers in width and length and are ideal for the long-term-monitoring conducted by meteorological services around the world. Typically, single- and dual-polarization data are used. Dual-polarization data were actively taken up for operational monitoring [4] and its use has demonstrated an improved discrimination between the open water and sea ice areas compared with single-polarization mode [5]. Within sea ice research, SAR images are used to estimate, e.g., ice drift [6], wave propagation into sea ice, ice concentration [7], and iceberg detection [8], [9]. The long data

record of single-polarization SAR missions means that most studies of SAR-based sea ice classification concentrate on such single polarized data [10]–[15]. These studies naturally concentrate on classical image analysis tools. The common tools are texture analysis via gray level co-occurrence matrices [10], [12], [16], autocorrelation methods [17], and Markov random fields [11]. Although useful and successful these techniques might be, there still remain major obstacles in sea ice classification for all mentioned approaches. Most prominent is the high variability of different ice types due to the influence of incidence angle, weather conditions, location, and season.

Polarimetric data (i.e., at least two channels available) promise to cope better with these obstacles, since each acquisition contains more information than only one SAR channel [18], [19]. The different backscatter behaviors in the channels allows for a better characterization of the ice types. Since the scenes are made up of multiple channels, information about the scattering mechanisms, which can be extracted from each scene, is used to complement the intensity values for a more accurate sea ice classification. When polarimetric data are available, parameters based on the eigendecomposition of the scattering matrix like the eigenvalues and components of the eigenvectors [20] or derived quantities like the canonical $H/A/\alpha$ parameters [20] are typically investigated. Reference [20] uses this approach on airborne L-band data to investigate the characteristics of sea ice types. In other approaches, the distributions of the coherency matrix are computed to be used as input arguments of an unsupervised Wishart classifier [21]. Recent publications [22]–[24] proposed a polarimetric approach based on the C-band data in which an automatic segmentation precedes a manual labeling of the segments. This automated method is then compared with manual segmentations and found to improve the consistency. Another study [25] compared spatially and temporally coincident fully polarimetric spaceborne C- and X-band data for sea ice characterization. For the most part, the aforementioned publications were concerned with directly relating the physical properties of certain ice types to particular polarimetric parameters and possibly giving physical explanations for observed behavior, and discussed how the generalizability of classifiers is impacted by location, season, and incidence angle. Here, we perform a comprehensive quantification of the polarimetric parameters derived from spaceborne fully polarimetric simultaneous SAR acquisitions in the L-, C-, and X-bands. The motivation is to establish a reliable automated sea ice classification algorithm for operational monitoring purposes from different frequency SAR sensors; therefore, we assess the information quality of the parameters prior to classification and validation. Instead of directly linking clusters in the parameter space to certain ice types, or physical properties of ice types, we instead train a neural network classifier. The neural network then implicitly encodes such relationships that exist between parameters and ice types with the help of expert knowledge and *in situ*/ancillary information.

The above discussions guide the structure of this paper. We will first introduce our spaceborne and airborne data sets and the polarimetric features. This is followed by an theoretic
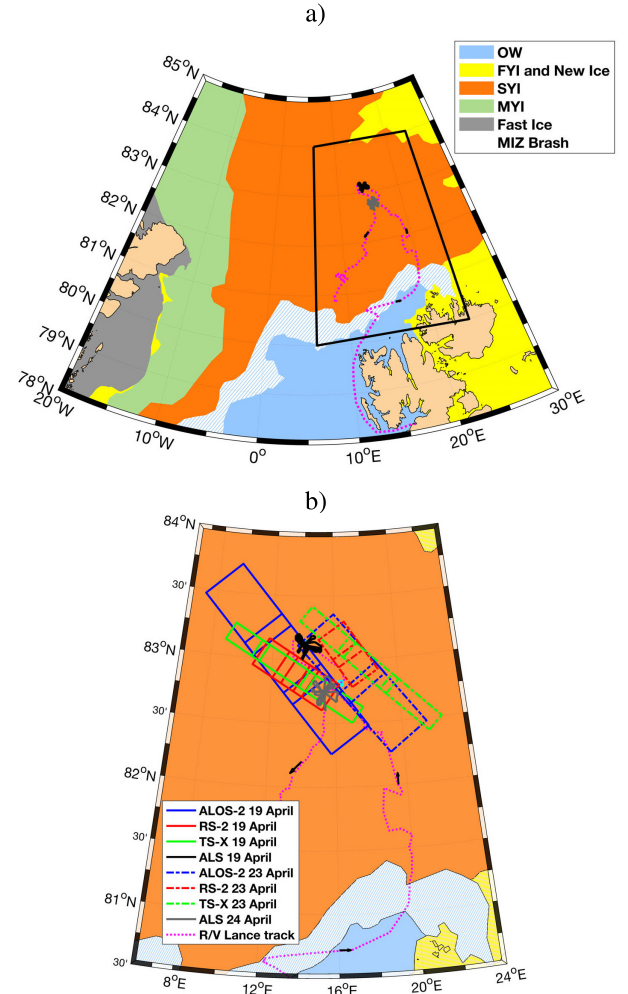

Fig. 1. Study area in the Arctic Ocean, north of Svalbard. (a) R/V *Lance*'s GPS track and the black box show the extent of zoomed-in view of map in (b). The color coding in the background is based on the WMO's ice type standard [30] and in addition the marginal ice zone is marked in white hashed with blue. The sea ice types were outlined and labeled by a sea ice analyze expert at the Norwegian Ice Service. (b) Zoomed-in view of map shows the satellite scene footprints. Black and gray patches: location of ALS acquisition from April 19 and April 24, 2015, respectively. Arrows: direction of R/V Lance's drift.

information analysis of the polarimetric features on all samples of training data sets, with the key statistical technique relying on the concept of mutual information [26]. By this analysis, we can quantify the redundancy and relevance of polarimetric features for the purpose of identifying different ice types. In Section III, we present the output of our subsequent pixel-based neural network classification and cross-compare the results with high-resolution airborne measurements. For the classification, we exploit an open source neural network library implemented in C (fast artificial neural network, see [27]), wherefore the reader is referred to standard literature on the theory and application of neural networks or to consult [28] and [29] for a successful use of neural network sea ice classification on SAR images.

II. DATA SET

A. N-ICE2015 Study Area and Meteorological Conditions

The study area is located in the Arctic Ocean north of Svalbard, between 82°N to 84°N and 6°E to 22°E (see Fig. 1).
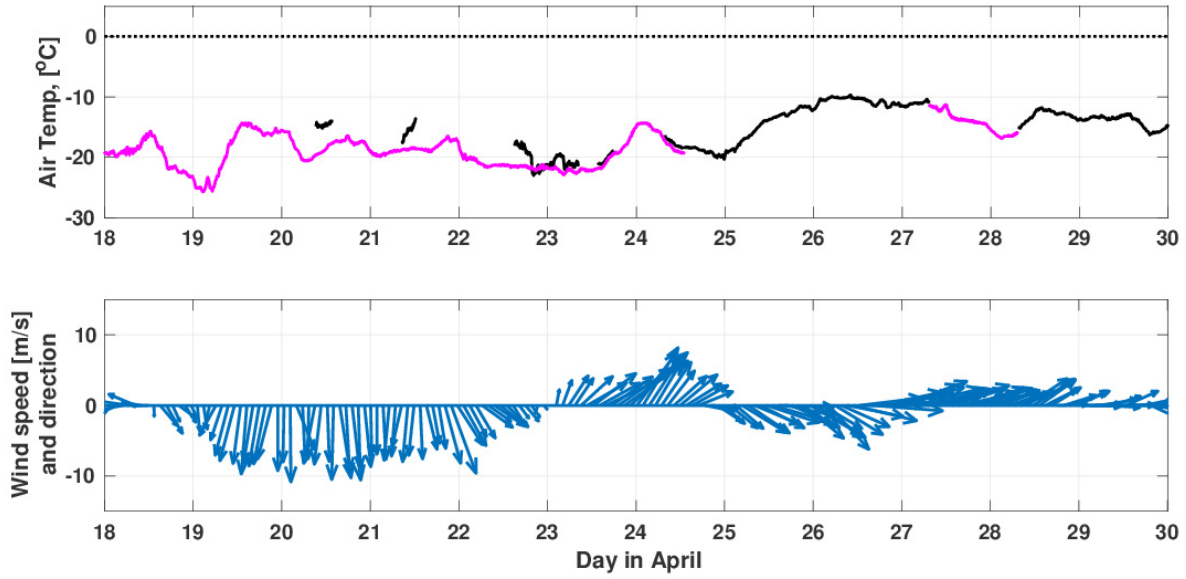
Fig. 2.   Air temperature and wind vector during the N-ICE2015 campaign (April 18, 2015 to April 30, 2015). Black lines: air temperatures measured on the sea ice. Magenta lines: temperatures measured on-board R/V *Lance*. Black dotted lines: 0 °C. The wind data were measured on the sea ice at 10-m height.

This region covers the subsea features of the Yermak Plateau north of Svalbard to the Nansen Basin further north. The Norwegian young sea ICE (N-ICE2015) drift field campaign lasted from January 12 to June 24, 2015 with the R/V *Lance* being anchored to, and drifted with, four different sea ice floes (referred to as "Floes" 1–4). When an ice floe, with which the ship was anchored, broke up, the ship was repositioned and moored to a new ice floe further north-east [31]. The satellite scenes used here were acquired over Floe 3. R/V *Lance* was anchored to Floe 3 from April 18 until June 5, 2015.

The total snow and ice thickness as well as the snow thickness was measured within 1–5 km of the position of R/V *Lance* at Floe 3. The mean snow and ice thickness was 1.79 m with a maximum thickness of 10.71 m and a minimum thickness of 0.11 m [32]. The modal snow and sea ice thickness was 1.56 m. The mean snow thickness for Floe 3 was 0.45 m with a maximum thickness of 1.58 m and a minimum thickness of 0 m [33]. The sea ice within the area surrounding R/V *Lance* during N-ICE2015 was primarily a mixture of FYI and second-year ice [34]. Even though there were also areas of nilas, young gray ice, young white ice, pancake ice, and frost flowers were often observed on the top of the young ice (YI) during the entire drift study. Sea ice type charts were provided by the Norwegian Ice Service for flight planning of the airborne laser scanner (ALS) flight and the map from April 22 is provided as background in Fig. 1. These charts were based on Sentinel-1A and Moderate Resolution Imaging Spectroradiometer images.

Air temperature was measured at 2 m a.s.l. with instruments mounted on a meteorological tower situated on the sea ice 300 to 400 m away from R/V *Lance* [35]. The air temperatures were measured with a Vaisala HMP155 (RM Young Model 43502) with the data being recorded every second and averaged over 1 min (for details see [35] and [36]). Air temperature was also measured every second on-board R/V *Lance* with an Aanderaa air temperature sensor

(model number 3455). The wind data were measured with a 2-D ultrasonic sensor (Lufft Ventus V200A-UMB) mounted at the meteorological tower at 10-m height. On-board R/V Lance at approximately 24-m height another wind sensor of the make Thies Clima 2-D ultrasonic was mounted. The primary weather measurements are the ones measured on the sea ice, and gaps in the data were replaced with weather data from the ship-based sensors (for details see [35] and [36]). The mean difference between the ice- and ship-based temperature sensors was small (0.18 °C with a standard deviation of 0.85 °C) (see Fig. 2 and [35]).

B. Fully Polarimetric SAR

The satellite data sets were acquired with high temporal and spatial correlation, at L-band (ALOS-2), C-band (RS-2), and X-band (TS-X). In the case of the ALOS-2, the acquisition mode is high-sensitive quad polarimetry (HBQ), and for RS-2 acquisitions, fine quad-pol (FQ). For TS-X, the images are StripMap (quad-pol) images. These X-band quad-pol data sets were acquired using the dual receive antenna (DRA) configuration mode, which is not yet commercially available [25]. In this paper, we want to explore sea ice classification on spaceborne multifrequency quad-polarimetric data, with secondary priority given to resolution, which naturally comes at the price of a smaller footprint. A list of the data taken with the respective technical details can be found in Table I and also in [24] and [25] (and figures therein). We remark that each acquisition from all the SAR sensors consists of two or three frames as presented in Fig. 1 (frame corresponds to nominal acquisition length in the azimuth direction). The images were acquired in the north of Svalbard between the latitudes 82.2°N and 83.8°N and longitudes 7°E and 23°E, which coincides with the previously described N-ICE2015 study region. Due to sea ice drift and different acquisition times for the different sensors, drift corrections have been

TABLE I

ALSO-2, RADARSAT-2 (RS-2), AND TERRASAR-X/TANDEM-X (TS-X) IMAGING MODES USED IN THIS PAPER. * DRA—DUAL RECEIVE ANTENNA (EXPERIMENTAL MODE). SM—STRIPMAP. FQ—FINE QUAD. HBQ—HIGH-SENSITIVE QUAD. Q—QUAD-POL

Date, Time (UTC)	Sensor	Incidence Angle	Polar. Mode	Imaging Mode	Slant Rg./ Az. Res.(m)	Footprint Az× Rg.	NESZ (dB)
2015/04/19, 13:16	TS-X	18.18°	Q*	SM	1.2 m / 6 m	115 km × 17.5 km	-18.78
2015/04/19, 14:51	TS-X	39.73°	Q*	SM	1.2 m / 6 m	115 km × 17.5 km	-16.21
2015/04/19, 13:19	RS-2	21.78°	Q	FQ	5.2 m / 7.6 m	75 km × 27 km	-34.20
2015/04/19, 20:32	ALOS-2	33.90°	Q	HBQ	5.1 m / 4.3 m	182 km × 42 km	-41.1
2015/04/23, 13:43	TS-X	27.20°	Q*	SM	1.2 m / 6 m	150 km × 17.5 km	-16.27
2015/04/23, 14:42	RS-2	37.25°	Q	FQ	5.2 m / 7.6 m	52.5 km × 27 km	-31.96
2015/04/23, 20:18	ALOS-2	33.90°	Q	HBQ	5.1 m / 4.3 m	127 km × 42 km	-41.1

ALOS-2 dataset were processed prior to the release of new radiometric and polarimetric calibration factors for the PALSAR-2 standard product on 24th March 2017.

applied to ALOS-2 and RS-2 acquisitions to a reference time defined by TS-X acquisitions, i.e., 13:17 UTC on April 19 and 13:43 UTC on April 23. The drift corrections were made with the assumption that R/V *Lance* drifted with the same speed and drift pattern as the mean sea ice drift for the area. The drift record from R/V *Lance*, sampled every second, was, therefore, used for the drift correction. In Fig. 2, we observe that the wind direction changes slightly between the satellite data and the ALS acquisitions, and rotational patterns within the sea ice pack were observed in [24] and [37]. The air temperature stays relatively stable during the data set acquisition time span (around −20 ± 5 °C, Fig. 2), and hence we can rule out any temperature related changes to the backscattering mechanism.

C. Airborne Laser Scanner

In this paper, we use, for the first time, ALS observations to validate the sea ice classification results obtained from polarimetric SAR imagery. The airborne survey was a part of the EU FP7 ICE-ARC project 2015 field campaign carried out with a British Antarctic Survey's (BAS) DHC-6 Twin Otter aircraft in cooperation with the Technical University of Denmark. The campaign was coordinated with the N-ICE2015 drift study and included two detailed surveys over the R/V *Lance* station at Floe 3 on April 19 and 24, 2015 [24], [31], [38]. Observations were also coordinated with helicopter-borne thickness sounding and supplemented with various satellite measurements, providing colocated data sets for extensive intercomparison and validation studies [24], [39].

The aircraft was equipped with an NIR (near infrared, 904 nm) laser and Ku-band radar altimeters, supplemented with kinematic geodetic global positioning system (GPS) and inertial navigation system (INS) attitude determination, along with atmosphere sounding and photography. For this paper, we use laser scanner measurements from the Riegl LMS-Q240i-80 laser scanner system transformed to surface elevations (referenced to the WGS 84 ellipsoid) using the GPS and INS information. This provides 3-D point cloud swaths of the surface, typically 400 m wide at the nominal flight altitude of 300 m. The full spatial resolution of the raw point cloud data is approximately 1 m × 1 m with a vertical accuracy

in the order of 0.1 m primarily depending on uncertainties in the kinematic GPS positioning. More details on the airborne campaign and data products are available in [38]—technical report about ALS data collection and processing.

For the validation of the SAR sea ice characterization, we use a derived product from the raw ALS point cloud measurements: the sea ice freeboards, which are defined as surface elevations (ice and snow) relative to the local sea level. These are obtained from a thinned (along track) and averaged (across track) data set with an approximate resolution of 5 m × 5 m. As a first step to identify the local sea level, a geoid model is subtracted from the ALS elevations giving orthometric heights, and here we use the recent update of the Arctic Gravity Project geoid model. A second step is needed to account for sea surface height variability caused by time varying ocean tides and currents, errors in the ocean mean dynamic topography, and measurement errors. This second step estimates an instantaneous sea surface elevation by identifying leads in the sea ice cover. Leads are found automatically by selecting the minimum values of the orthometric heights within equidistant subsections. The typical subsection length is 5 km, which is chosen based on local ice properties and geoid model variations and resolution. Finally, the instantaneous sea surface is estimated by a linear fit of minimum values with outlier rejection, smoothed by least-square collocation, and then subtracted from the thinned and averaged data providing sea ice freeboards (see also [40] for more details). This method relies on the existence of leads in sea ice pack otherwise it will underestimate the freeboard heights. Manual examination of the data set supports the presence of leads at 5-km-length scale but also revealed an offset of 0.2 m, which was removed.

Figs. 3 and 4 show the dense areal coverage of the ALS freeboard data set. The data have been corrected for local drift during the survey by assuming that the sea ice drifts with the same speed and direction as the R/V *Lance* and also with negligible rotation and deformation in the time period. The drift correction is done using the recorded ship position every minute estimating a linear drift between each positon and using this to transfer (drift) the data set to the reference time of 13:17 UTC on April 19 and 13:43 UTC on April 23. The ALS freeboard measurement and SAR acquisitions show
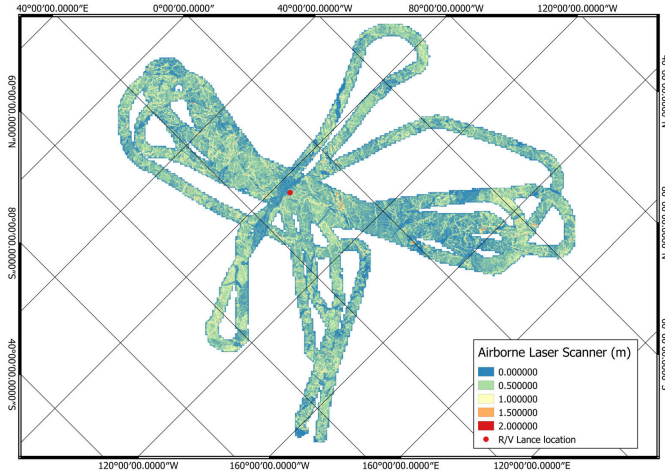
Fig. 3. Overview of ALS data acquisition during the N-ICE2015 Campaign on April 19, 2015 at 10:32 UTC. Location of R/V *Lance* indicated with a red point at the center.
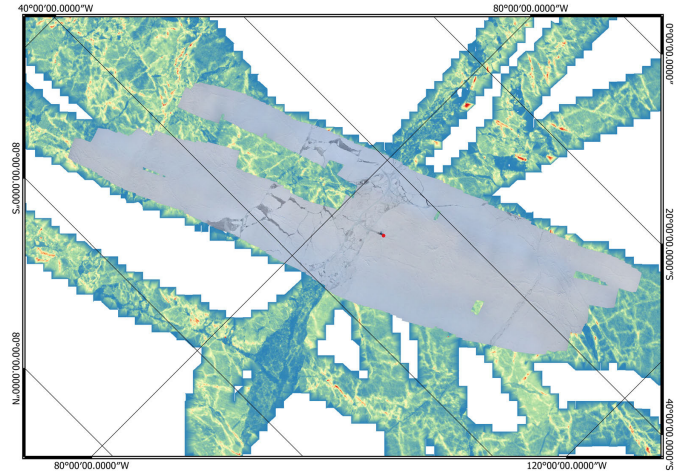

Fig. 5. Overview of drift corrected optical image acquisition from the BAS aircraft during the N-ICE2015 Campaign on April 19. Corresponding ALS acquisition as background.
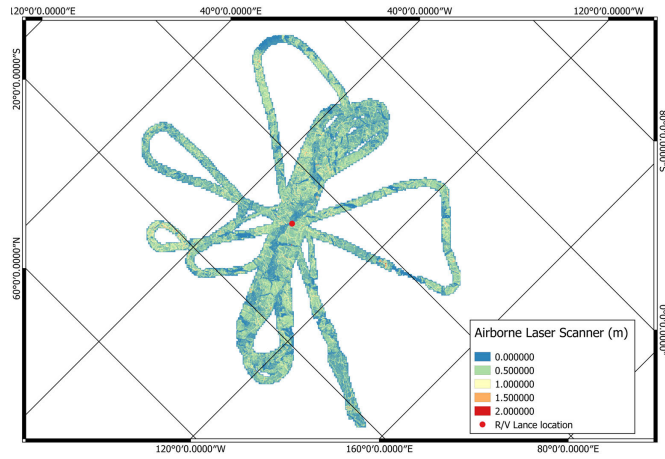

Fig. 4. Overview of ALS data acquisition during the N-ICE2015 Campaign on April 24, 2015 at 09:55 UTC. Location of R/V *Lance* indicated with a red point at the center.
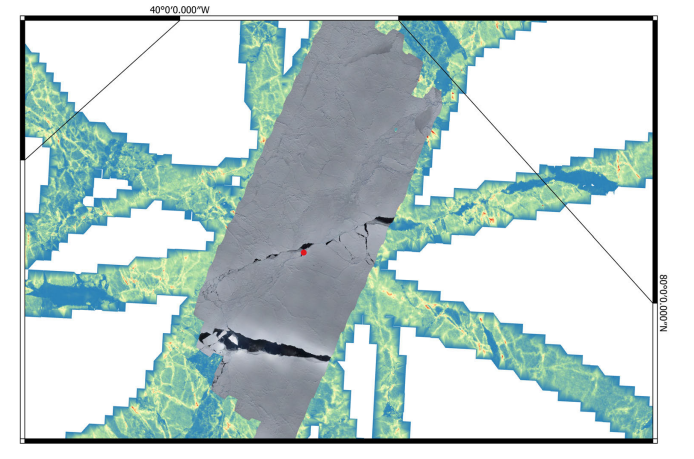

Fig. 6. Overview of drift corrected optical image acquisition from the BAS aircraft during the N-ICE2015 Campaign on April 24, 2015. Corresponding ALS acquisition as background.

good colocation agreement after the drift correction verifying the assumptions.

D. High-Resolution Photograph Mosaic

The aerial photographs were acquired by an Intergraph Z/I Imaging Digital Mapping Camera that is mounted on the BAS DHC-6 Twin Otter. Image acquisitions were carried out simultaneously with the ALS acquisition. The individual images were corrected for drift and stitched into daily mosaic images. Georeferencing, and colocation, to the satellite images was performed using the Georeferencer function of QGIS by manually matching clearly identifiable features between the different image data sets. Figs. 5 and 6 show the areal coverage of the mosaicked photograph along with the location of the R/V *Lance*. As mentioned previously, the drift correction is performed using the recorded ship position, to the reference time of 13:17 UTC on April 19 and 13:43 UTC on April 23. All satellite and airborne data sets presented in this paper are projected into NSIDC polar stereographic projection.

III. METHODOLOGY

Our proposed methodology consists of two steps. First, we extract for each pixel a vector of 18 polarimetric features, with these 18 values for each pixel referred to as the "vector." This is followed by the selection of training/validation patches for the artificial neural network (ANN) classifier. A detailed description of the 18 polarimetric features used in this paper, along with their mathematical definitions, can be found in (3)–(23).

In this paper, we present a quantitative evaluation of sea ice classification results obtained from spaceborne L-, C-, and X-band quad-polarimetric acquisitions and validate them incorporating high-resolution (with large spatial extent) airborne measurements. As an established standard [24], [25], we will train the ANN to classify each image in four different classes, i.e., open water and nilas (OW), YI, smooth FYI(SFYI), and rough first year/multiyear ice (RFYMYI). As mentioned before, during the selection of training/validation patches, we mainly relied on ground truth

from airborne data sets (ALS and high-resolution optical photographs), as well as ice charts, ice concentration map, expert visual judgment of the Pauli RGB compositions, and polarimetric feature images. Aforementioned information was analyzed manually to generate training and validation patches. It is also important to note here that the training/validation patches were selected in such a way that they adequately represent the incidence angle variation from near to far range. Each vector is then fed into a neural network classifier for the purpose of training and validation [25]. In order to minimize noise effects, we employed a 5×5-pixel median filter on all the polarimetric features. And before ingesting in a neural network, all features must be rescaled into the range $[-1.0, 1.0]$. A common nonlinear rescaling method involves the tanh function

$$\tilde{x} = \tanh\left(\frac{x - \overline{X}}{\nu_X}\right) \qquad (1)$$

where $\overline{X}$ denotes the mean of all values of feature X in the training data and ν_X denotes the standard deviation of all values of feature X in the training data. After a neural network has been trained on data rescaled with these particular training data statistical parameters $\mathcal{P} = \{\overline{X}, \nu_X\}$, any feature vector that is fed into this network for classification must be rescaled in the same fashion with these parameters $\mathcal{P}$ before classification. The entire statistical analysis (in Section IV-A) will be conducted on the rescaled feature values, since they determine the behavior of the classifier.

In all frequency bands, the copol power ratio (γ) has been proven to be an excellent measure to distinguish open water and all other ice types, in particular older and thicker ice types [41]–[44], provided that the incidence angle is not too low (according to [42] above $27°$ for the C-band), and wind speeds are low to moderate (less than 14 m/s in the C-band according to [42]). In the case of younger ice types, the copol power ratio is not as powerful in discriminating thin ice from open water. The C-band copolarized phase difference $\Delta\phi$ was found to be useful for discriminating certain thinner ice types [22], [41], [45]. For the L-band, the quad-polarimetric entropy, $H^{(q)}$, is known to discriminate open water from ice types generally well and also thin ice from thick ice types due to the underlying different scattering mechanisms [20]. Quad-polarimetric L-band anisotropy, $A^{(q)}$, is known to be sensitive to surface roughness [20].

IV. FEATURE ANALYSIS AND CLASSIFICATION RESULTS

Since we want to study the suitability of polarimetric features for sea ice classification, we will first briefly discuss the visual interpretation of the information content of some features. Thereafter, we analyze the information content of each feature and their redundancy with respect to sea ice classification.

A. Mutual Information Analysis, Relevance, and Redundancy

In order to obtain a first impression about the predictive quality of the different features, i.e., their ability to separate different ice classes, we display all of them

in Fig. 7. For consistency, we will, throughout this paper, display the results from the ALOS-2 scenes from April 23. The feature images are depicted in slant range. Since the features are extracted in this format, the classification is also performed in the slant range and later projected to ground range. Therefore, the reader is cautioned to notice that the images in Section IV-B are displayed in ground range and thus appear slightly distorted (due to the ground range projection). When inspecting visually, some features [e.g., γ, μ, δ, τ, and span$^{(d/q)}$] can already be observed to contain adequate information about the sea ice situation. For all the frequency bands, the copol power ratio allows us to clearly discriminate open water/nilas (OW) portions. In the case of ALOS-2, the structure rich features of δ, τ, $H^{(d)}$, $H^{(q)}$, $\lambda_i^{(d)}$, span$^{(q)}$, span$^{(d)}$, and μ allow us to directly discriminate different ice floes and ice types, especially for discriminating open water (OW) and YI. For the C- and X-band acquisitions, it was observed that $\lambda_i^{(d)}$, span$^{(q)}$, span$^{(d)}$, and μ provided good separation between the different ice types. For the ALOS-2 scenes, span$^{(q)}$ and μ are observed to be useful for discriminating SFYI and first year/multiyear ice (RFYMYI), i.e., it contains information about the degree of deformation. Nonetheless, the same polarimetric features have subjectively the richest visual information content for all the investigated frequencies. Therefore, in this section, we evaluate each feature's statistical information content.

In order to quantify the information content of polarimetric features, we apply the concept of mutual information from information theory, which has become an important measure in the analysis of informational content and discriminative power [26], [46]. The statistical information was extracted based on the training rectangles which were previously selected for the ANN training. In our case, the major challenge lies in the image size at full resolution; in the case of ALOS-2 and TS-X, one full-resolution purely complex image layer occupies about 1400 MB of RAM per complex image channel, i.e., 6.3 GB for the full scattering matrix. For an RS-2 scene, the corresponding size is 500 MB. Given that this memory consumption multiplies with the number of (real-valued) polarimetric features, the advantage of analyzing the relevance and redundancy of features and accordingly decimating the feature set before classification is clear for developing operational services.

Given two random variables X and Y, the mutual information $\mathcal{I}$ of these variables is defined as

$$\mathcal{I}(X|Y) = \mathcal{H}(X) - \mathcal{H}(X|Y) \qquad (2)$$

where $\mathcal{H}(\mathcal{X})$ denotes the entropy of X and $\mathcal{H}(X|Y)$ denotes the conditional entropy of X given Y. Details can be found in [26] and [46]. The intuitive concept behind this definition of $\mathcal{I}$ describes the fraction of information that is shared mutually by both X and Y, i.e., their "information overlap." In other words, a higher value of $\mathcal{I}(X|Y)$ allows us to infer more information about X from prior knowledge of Y. Thus, one can quantify, in an information theoretical sense, the (nonlinear) information correlation of X and Y. As one would expect for the intuitive concept of "shared information,"
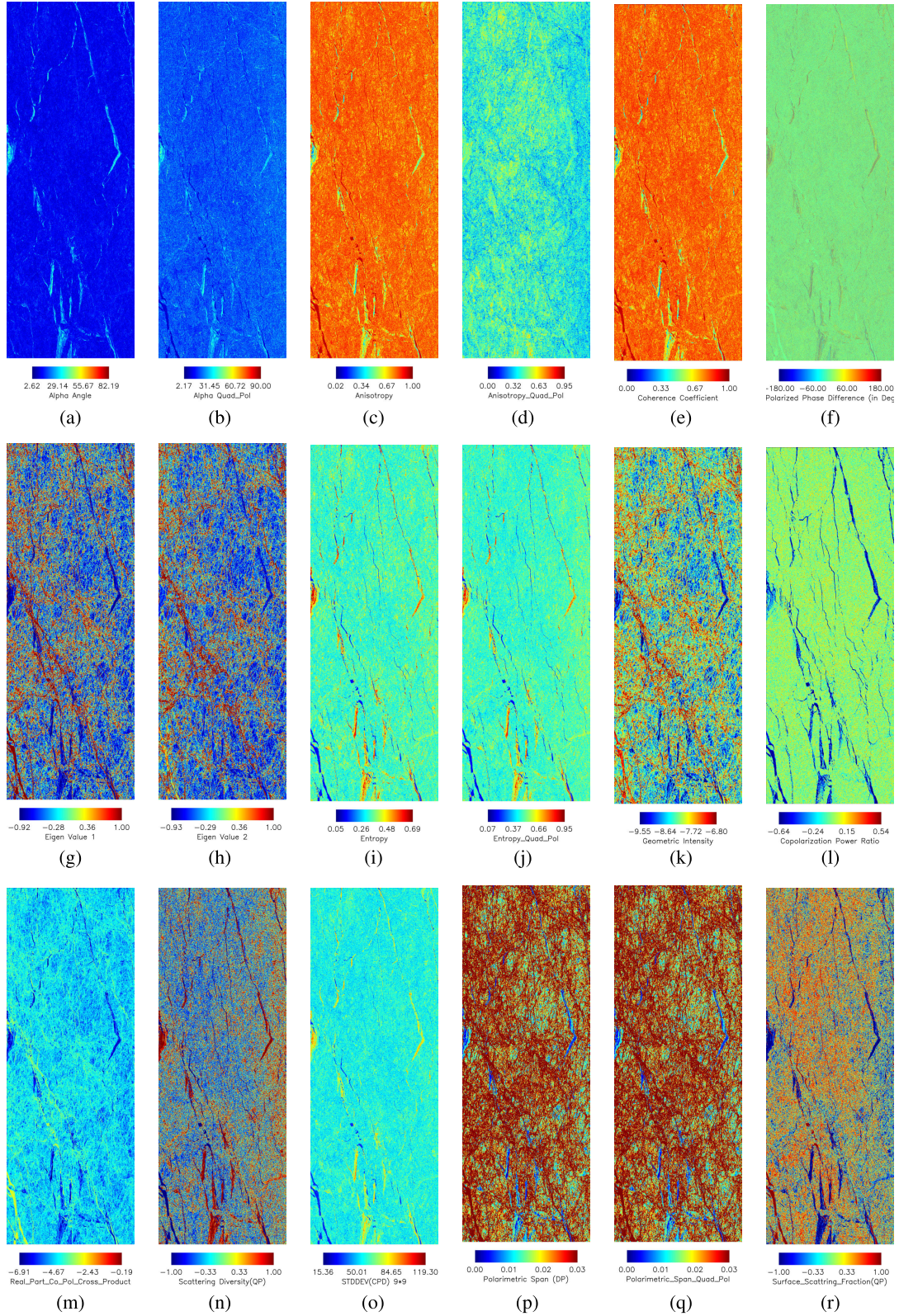
Fig. 7. Visual representation of different polarimetric features for ALOS-2 on April 23, 2015. (a) $\alpha^{(d)}$. (b) $\alpha^{(q)}$. (c) $A^{(d)}$. (d) $A^{(q)}$. (e) ε. (f) $\Delta\phi$. (g) $\lambda_1^{(d)}$. (h) $\lambda_2^{(d)}$. (i) $H^{(q)}$. (j) $H^{(q)}$. (k) μ. (l) γ. (m) ρ. (n) δ. (o) $Var\,\Delta\phi$. (p) span$^{(d)}$. (q) span$^{(q)}$. (r) τ.

the mutual information $\mathcal{I}(\mathcal{X}|\mathcal{Y})$ is symmetric in X and Y also in a strictly mathematical sense, i.e., $\mathcal{I}(X|Y) = \mathcal{I}(Y|X)$. Since $\mathcal{I}$ is dimensionless, we employ it only to juxtapose

and rank different features. We will, therefore, not investigate the absolute value of $\mathcal{I}$ in this paper. Henceforth, we will employ the following parlance for particular choices of X

and Y. In this case, X is the class information and Y is a feature (X attains, e.g., OW, YI, SFYI, and RFYMYI), with a (relatively) high mutual information $\mathcal{I}$ implying a strong predictive value of feature Y for telling the class X. Utilizing the symmetry of $\mathcal{I}$, class X can reliably foretell the predictive value of feature Y. When X is set to only attain a pair of classes [i.e., only data from two classes are used for computing $\mathcal{I}(X|Y)$], the resulting $\mathcal{I}$ measures the suitability of Y to discriminate those two particular classes. We then use such a configuration (Y feature and X all classes or two classes a and b) to rank the features according to relevance (all-class-relevance and two-class-relevance). The notation shall be $\mathcal{I}(Y|Class(all))$ or $\mathcal{I}(Y|Class(a,b))$ for named configurations.

For a different purpose, we let X and Y be two different features. In the case $\mathcal{I}(X|Class(all))$ and $\mathcal{I}(Y|Class(all))$ are roughly the same (i.e., have equal relevance) with high mutual information, we define $\mathcal{I}(X|Y)$ to imply high redundancy. This redundancy can then be used to prudently decimate the set of features that is used in classification for operational purposes. In this particular publication, we will, however, not present any neural network that ingests only a pruned feature set, but set up the neural network topology with all available features. Pruned feature sets will be exploited further in the future work (see also elaboration in Section IV-B).We normalize $\mathcal{I}(X|Y)$ by dividing by $\sqrt{\mathcal{H}(X)}$, in order to achieve increased comparability.

The all-class-relevance $\mathcal{I}(X|class(all))$ for the ALOS-2 (April 23) acquisition can be found in Table II. We observe in this table that the features $\lambda_1^{(d)}$, ε, span$^{(d)}$/span$^{(q)}$, ρ, and $A^{(d)}$ are in the upper third of the all-class-relevance ranking. τ and δ also appears to be in the upper half of the table. The features δ and $H^{(q)}$, which always appear as direct successors in mentioned tables, range in the midfield (similar to the C- and X-band results in [25]). We find $\alpha^{(q)}, \alpha^{(d)}, \Delta\phi, Var\Delta\phi$, and mostly of rather low all-class-relevance. The feature γ ranked in the low midrange for the incidence angle of 33.90° was previously found to be strongly dependent on the incidence angle, with high all-class-relevance for far range acquisitions and lower relevance with decreasing incidence angle [25], [42]. It might also be due to the fact that, although γ provides satisfactory information while discriminating OW and other types of sea ice, it provides very little information on discrimination between different ice classes (e.g., between SFYI and RFYMYI, see Table III).

For the evaluation of the feature redundancy for ALOS-2, Fig. 8 shows some strong information theoretic correlations, particularly between $H^{(q)}$ and δ and between $H^{(d)}$ and $A^{(d)}$ among others. These two particular redundancies were also observed for the C- and X-band data sets. Other feature pairs which have strong information theoretic correlations are ρ and span$^{(d/q)}$, ρ and $\lambda_1^{(d)}$, ε and $H^{(d)}$, ε and $A^{(d)}$, span$^{(d)}$ and $\lambda_1^{(d)}$, and expectedly between span$^{(q)}$ and span$^{(d)}$. The observation that γ is important for the discrimination of open water from thick ice types has been made before for different bands [43]. For the purpose of navigation through ice-infested waters, this discrimination is of crucial importance.

TABLE II

ALOS-2, APRIL 23, 2014: RELEVANCE FOR DISTINGUISHING ALL DIFFERENT CLASSES (ALL-CLASS-RELEVANCE). $\mathcal{I}_0$: $\mathcal{I}(X|Class(all))$. $\mathcal{I}_1$: $\mathcal{I}(X|Class(all))/\sqrt{\overline{\mathcal{H}(X)}}$

Feature	$\mathcal{I}_0$	$\mathcal{I}_1$
$\lambda_1^{(d)}$	1.3555593	0.63543047
ε	1.3809887	0.62798483
$span^{(d)}$	1.3304048	0.62172027
ρ	1.3794360	0.61706503
$span^{(q)}$	1.3221922	0.61688799
$A^{(d)}$	1.3496956	0.61337800
$H^{(d)}$	1.3499795	0.60993402
τ	1.3336358	0.60310914
δ	1.2982471	0.59232067
$H^{(q)}$	1.2889631	0.58744506
μ	0.99093687	0.44160534
$\alpha^{(d)}$	0.96775274	0.43119251
γ	0.90314771	0.40320415
$\alpha^{(q)}$	0.90686615	0.39787452
$A^{(q)}$	0.27211726	0.25624728
$\lambda_2^{(d)}$	0.57964567	0.11875189
$Var\Delta\phi$	0.13399555	0.058586150
$\Delta\phi$	0.13399555	0.0.058586150

Hence, γ and δ can be considered indispensable for the proposed L-band data set classification scheme.

We now summarize our findings and state the essence of our relevance and redundancy analysis. For both RS-2 and TS-X acquisitions, we found similarly high relevance for a number of lexicographic features and likewise rather low relevance for Pauli-based features [25]. On the other hand for the L-band data set, some Pauli-based features, such as $H^{(d)}$ and $A^{(d)}$, were found to perform well. In contrast to observations at the C- and X-bands, ε and τ performed exceptionally well for the L-band specifically in the case of discriminating YI from other types of ice (see Table III).

In Section IV-C about classification results, we have conducted the classification with all features, i.e., we have included all features despite the possible redundancies we found. For future applications, we will more rigorously investigate the performance of different subsets of features. As hinted at during the discussion of the visual impression of the feature images, we emphasize again that our findings about relevance and redundancy and possible recommendations for feature choice could not have been easily and reliably obtained without the mutual analysis-based treatment. By the spatial coincidence of both TS-X and RS-2

TABLE III
ALOS-2, APRIL 23, 2014: TWO-CLASS-RELEVANCE IN DESCENDING ORDER FOR DIFFERENT PAIRS OF CLASSES. CLASS INDICES ARE AS FOLLOWS. 1: OW. 2: YI. 3: SFYI. 4: RFYMYI

1 *vs.* 2	1 *vs.* 3	1 *vs.* 4	2 *vs.* 3	2 *vs.* 4	3 *vs.* 4
δ	δ	γ	τ	ε	μ
$H^{(d)}$	$H^{(q)}$	$H^{(q)}$	$\alpha^{(d)}$	τ	$span^{(q)}$
$H^{(q)}$	γ	δ	ε	$A^{(d)}$	$span^{(d)}$
$A^{(d)}$	$\lambda_1^{(q)}$	$H^{(d)}$	$H^{(q)}$	$H^{(d)}$	$\lambda_1^{(q)}$
ε	$span^{(d)}$	$A^{(d)}$	δ	ρ	ρ
τ	$H^{(d)}$	ε	γ	δ	$\lambda_2^{(q)}$
ρ	$span^{(q)}$	τ	$H^{(d)}$	$H^{(q)}$	$A^{(q)}$
$\lambda_1^{(q)}$	ρ	$\alpha^{(d)}$	$A^{(d)}$	$\lambda_1^{(q)}$	$A^{(d)}$
$span^{(q)}$	$A^{(d)}$	$\lambda_1^{(q)}$	$\alpha^{(q)}$	$span^{(d)}$	$H^{(d)}$
$span^{(d)}$	ε	ρ	ρ	$span^{(q)}$	ε
μ	τ	$span^{(d)}$	$\lambda_1^{(q)}$	$\alpha^{(d)}$	τ
$\alpha^{(q)}$	μ	$span^{(q)}$	$span^{(d)}$	μ	δ
$\lambda_2^{(q)}$	$\alpha^{(d)}$	$\alpha^{(q)}$	$span^{(q)}$	γ	$H^{(q)}$
$\alpha^{(d)}$	$\alpha^{(q)}$	μ	μ	$\lambda_2^{(q)}$	$\alpha^{(q)}$
γ	$\lambda_2^{(q)}$	$A^{(q)}$	$\lambda_2^{(q)}$	$A^{(q)}$	$\alpha^{(d)}$
$Var\Delta\phi$	$Var\Delta\phi$	$\lambda_2^{(q)}$	$Var\Delta\phi$	$A^{(q)}$	$Var\Delta\phi$
$\Delta\phi$	$\Delta\phi$	$Var\Delta\phi$	$\Delta\phi$	$Var\Delta\phi$	$\Delta\phi$
$A^{(q)}$	$A^{(q)}$	$\Delta\phi$	$A^{(q)}$	$\Delta\phi$	γ

Fig. 8. Normalized mutual information for ALOS-2 image on April 23, 2015, $\mathcal{I}(Y_1, Y_2)/\sqrt{\mathcal{H}(Y_1)\mathcal{H}(Y_2)}$. Features are as follows. 1: γ. 2: $\Delta\phi$. 3: ρ. 4: ε. 5: μ. 6: τ. 7: $span^{(q)}$. 8: δ. 9: $H^{(q)}$. 10: $A^{(q)}$. 11: $\alpha^{(q)}$. 12: $span^{(d)}$. 13: $H^{(d)}$. 14: $A^{(d)}$. 15: $\alpha^{(d)}$. 16: $\lambda_1^{(d)}$. 17: $\lambda_2^{(d)}$. 18: $Var\Delta\phi$.

acquisitions, any randomness in the findings due to different locations and hence dominant ice types can be precluded. This underscores the general validity of the observed similarity for TS-X and RS-2 images concerning the redundancy and relevance for ice classification (despite different incidence angles).

B. Classification Results

The results of the proposed classifier can be seen in Figs. 9–11, respectively, for L-, C- and X-band acquisition on April 23. Next to these images, we also display for comparison the Pauli RGB composites of the acquisitions. In order to validate the stability of the training process, we randomly split the initial training data patches into two mutually exclusive subsets, i.e., training data set and validation data set. Although it is typical to perform an N-fold test, where multiple random divisions of training data set and validation data set are performed to achieve an optimal trained network, we restrict ourselves to simple random split as it was outside the scope of this paper. The classification results compared to validation data samples as presented in Table IV exhibit a very promising accuracy, which underscores the stability of our algorithm. The percentages in the matrix indicate the proportion of
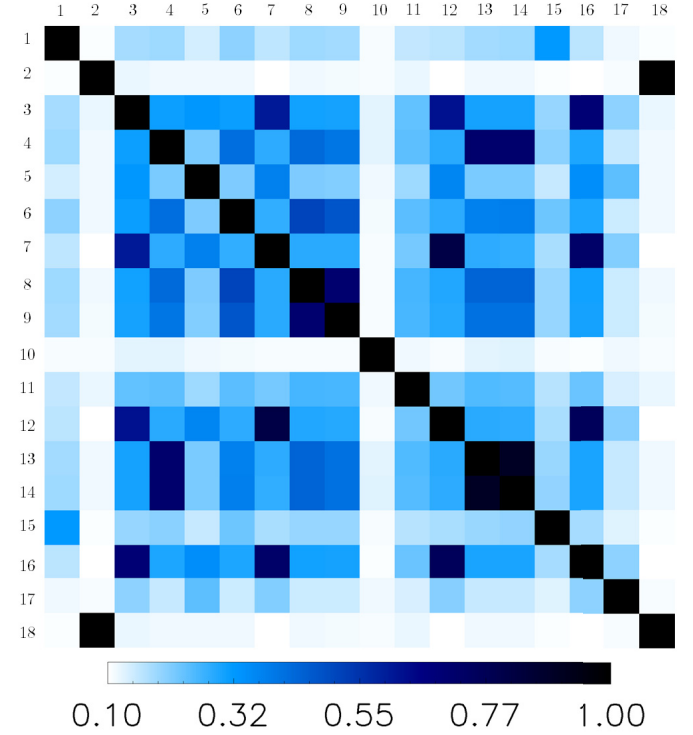
samples of one reference class that were assigned to the respective ice type by the classifier. Therefore, columns add up to 100%. The results for the ALOS-2 April 23 acquisition are presented in Fig. 9, with maximum inaccuracy of 3.1% (SFYI) in the following accuracy matrix. In [25], confusion matrices for the C- and X-bands were reported with approximately similar overall accuracy compared with the results in Table IV.

A strong match between the visual structures in these Pauli RGB images and the pertaining classified images can be observed for all frequency bands. Open water/nilas areas are clearly detected throughout for all frequency bands. In addition, the YI portions are classified correctly except for a slight over representation in the far range for TS-X acquisitions. This is most likely due to a noticeable noise pattern (especially on the vertical margins) of some TS-X acquisitions. Such noise pattern-related biases certainly need to be addressed when establishing the classifier (minimum σ_0 measurable by TS-X DRA quad-pol imaging mode is around -16 to -19 dB). Fig. 12 shows a prominent portion of YI area in the L- and C-bands, where ALOS-2 produced significantly a better characterization compared to RS-2 acquisition on April 23. In this example, we can also observe a small portion of open water (in blue) within the YI part (in purple) that is characterized correctly. SFYI portions, which appear as darker ice floes in the Pauli RGB composite images, are also correctly detected, as well as the bright structures of more strongly deformed FYI. Furthermore, a fairly reasonable
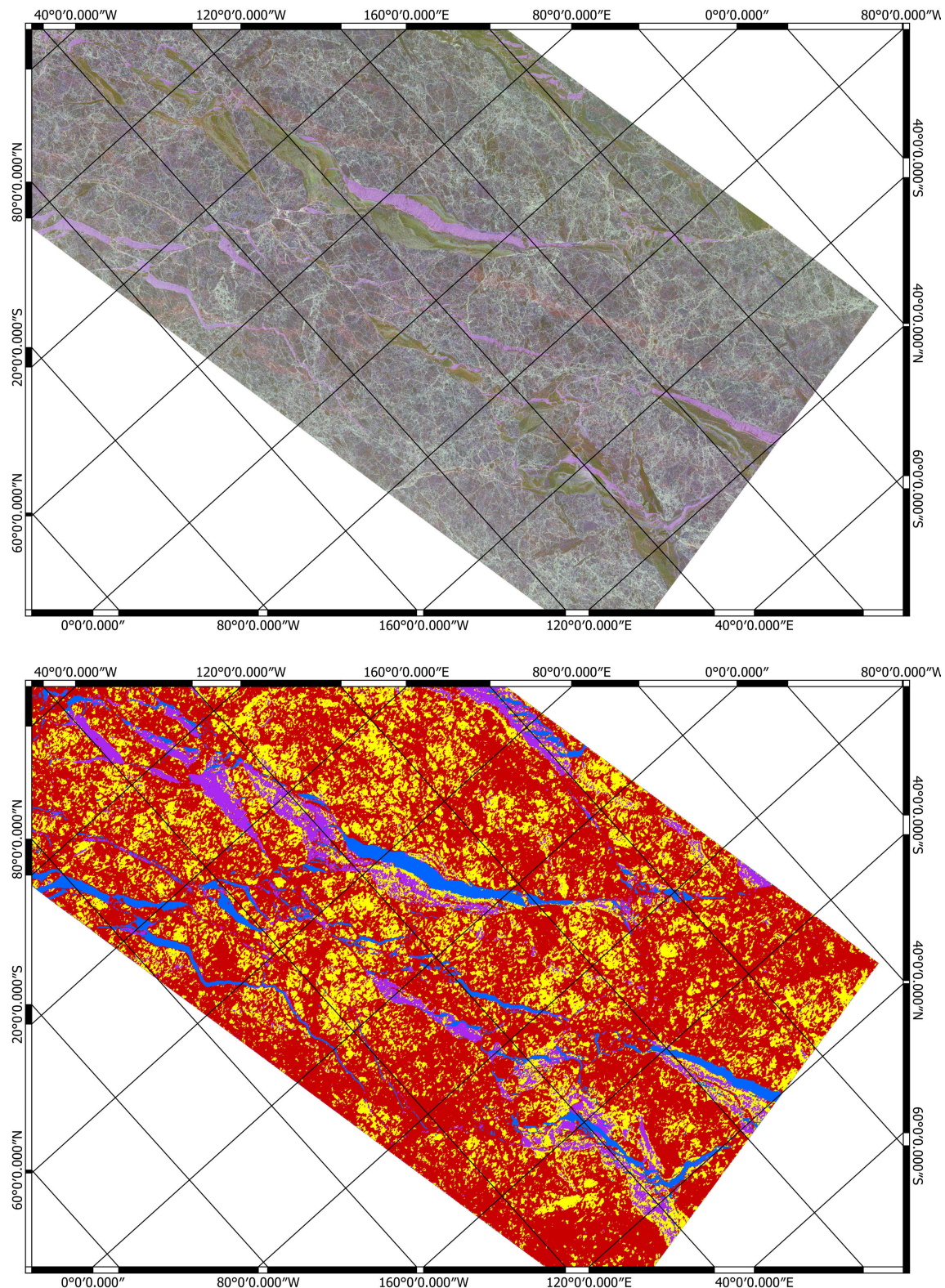
Fig. 9. (Top) Geocoded Pauli RGB composite (red: HH-VV, green: HV + VH, and blue: HH + VV) of the ALOS-2 acquisition on April 23, 2015. (Bottom) Ice classification on ALOS-2 acquisition. Blue: open water/nilas (OW). Purple: YI. Yellow: SFYI. Red: RFYMYI.

degree of correspondence has been achieved between *in situ* airborne measurement and classified ALOS-2, RS-2, and TS-X imagery, which are discussed in more detail in Sections IV-C and V.

C. Validation of Classification Results With Airborne Measurements

The classified sea ice types are here compared to the overlapping high-resolution airborne measurements, e.g., the ALS
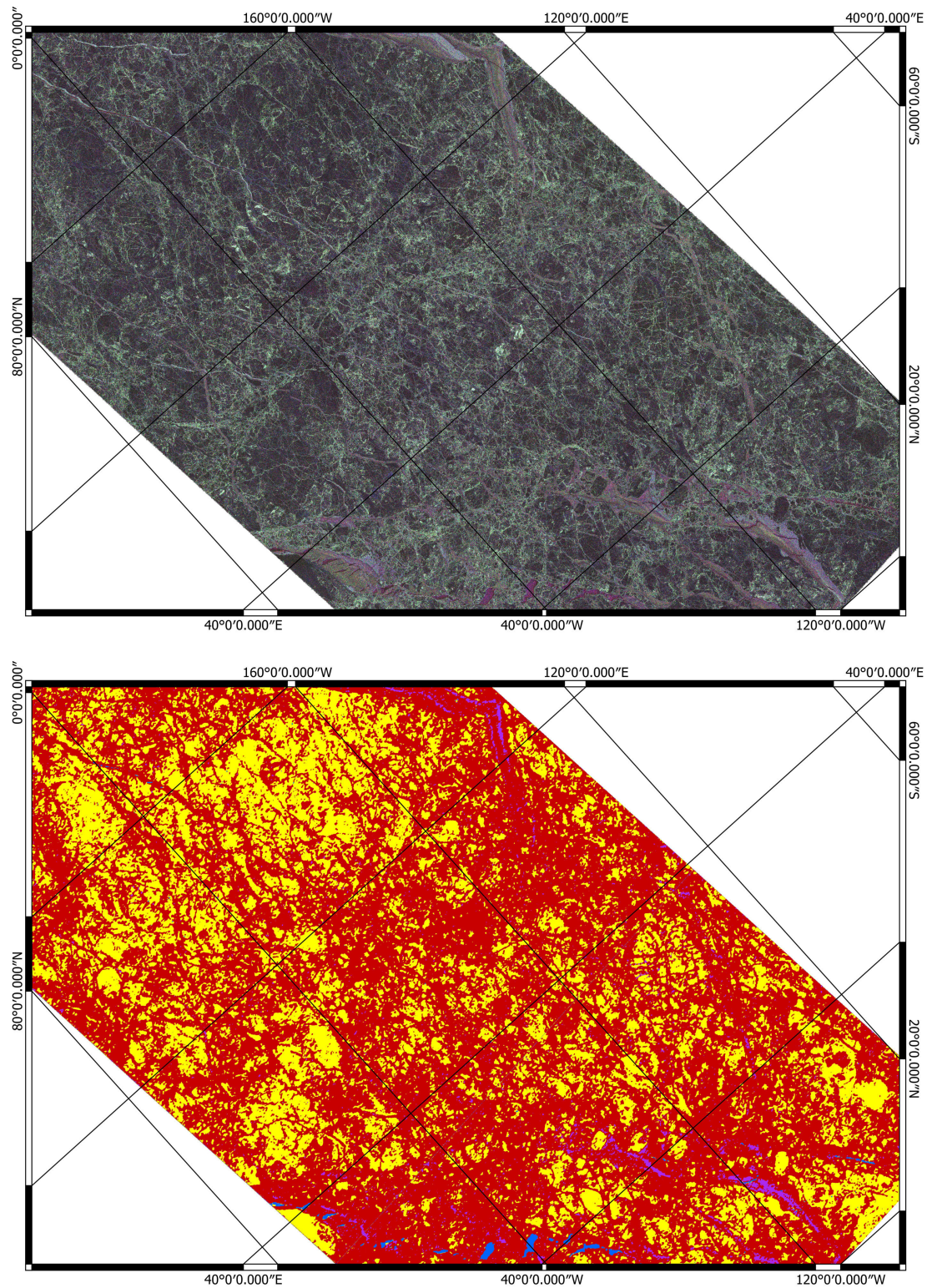
Fig. 10. (Top) Geocoded Pauli RGB composite (red: HH-VV, green: HV + VH, and blue: HH + VV) of the RS-2 acquisition on April 23, 2015. (Bottom) Ice classification on RS-2 acquisition. Blue: open water/nilas (OW). Purple: YI. Yellow: SFYI. Red: RFYMYI.

freeboard measurements and the photograph mosaics. This kind of comparisons of SAR-based sea ice classification results, with comparable resolution to SAR acquisitions, is rare due to the challenging nature of the Arctic environment and

high associated costs for airborne measurements. In order to validate our results, all satellite and airborne measurements are linearly drift corrected to the reference times of 13:17 UTC on April 19 and 13:43 UTC on April 23 using the GPS track of
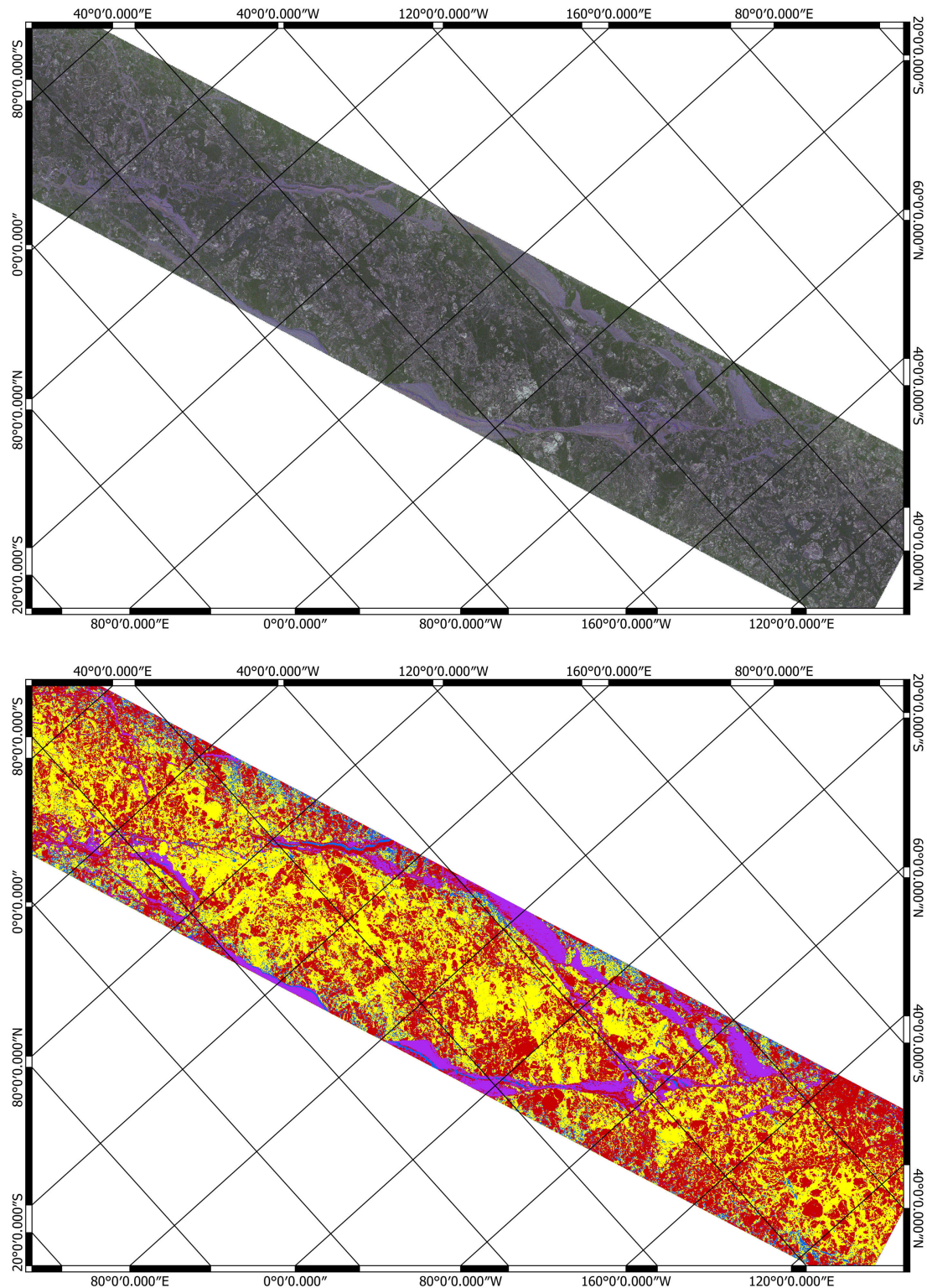
Fig. 11. (Top) Geocoded Pauli RGB composite (red: HH-VV, green: HV + VH, and blue: HH + VV) of the TS-X acquisition on April 23, 2015. (Bottom) Ice classification on TS-X acquisition. Blue: open water/nilas (OW). Purple: YI. Yellow: SFYI. Red: RFYMYI.

R/V *Lance* together with cross-reference to the high-resolution aerial photographs. Due to the high sea ice concentration over the study region as well as the tightly packed ice, we expected that there was no substantial large-scale rotation of floes in relation to each other within the time span of the respective data sets acquisition. However, it is worth mentioning here that the colocation of SAR scenes and airborne measurements has minor inconsistencies due to the nonlinear movement of the
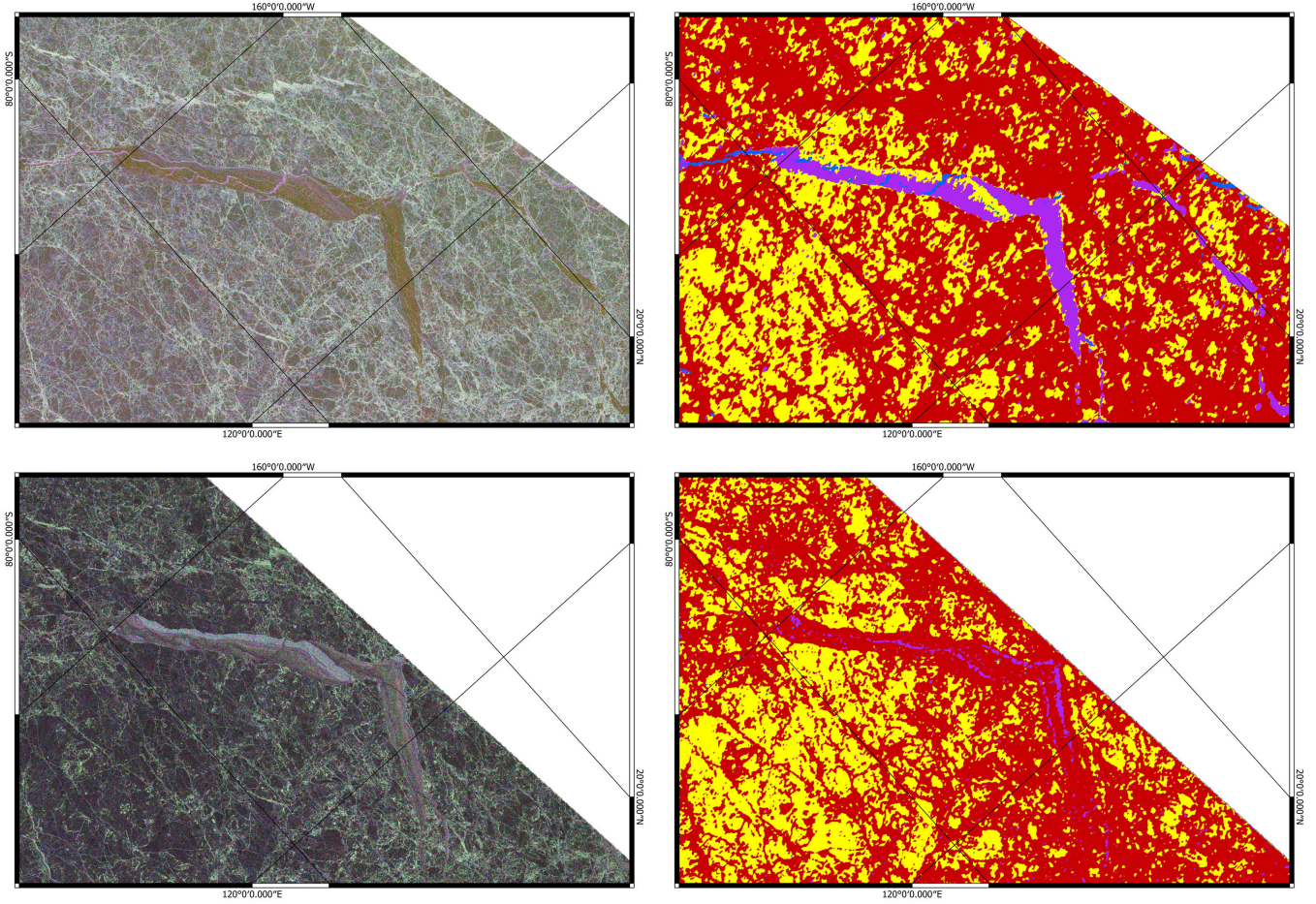
Fig. 12.   (Left) Geocoded Pauli RGB composite (red: HH-VV, green: HV + VH, and blue: HH + VV) of the ALOS-2 and RS-2 acquisition on April 23, 2015. (Right) YI representation on ALOS-2 and RS-2 acquisition on April 23, 2015. Blue: open water/nilas (OW). Purple: YI. Yellow: SFYI. Red: RFYMYI.

TABLE IV

CLASSIFICATION RESULTS COMPARED TO REFERENCE DATA SAMPLES FROM EACH CLASS, AVERAGED OVER DIFFERENT NEURAL NETWORK TOPOLOGIES, ALOS-2 ACQUISITION ON APRIL 23, 2015

	Reference ice class			
ANN Result	OW	YI	SFYI	RFYMYI
OW	100.0%	0%	0%	0%
YI	0%	97.3%	0%	0%
SFYI	0%	0%	96.9%	3.0%
RFYMYI	0 %	2.7%	3.1%	97.0%

floes especially near the OW and YI portions, although this will have only insignificant effect on our analysis.

To relate the ALS freeboard measurements to the sea ice thickness (T), [47] and [48] found that the ALS freeboard values (h_f) should be multiplied with a factor k, where k depends on the sea ice, snow, and water density and the sea ice and snow height

$$T = k \times h_f. \tag{3}$$

A more detailed study in [49] found that for YI the k-value is 1–2, for level ice the k-value is equal to 4.4, and for

deformed ice the k-value is equal to 5.2. Manually selected ROIs were used to extract σ_{HH} and ALS freeboard values from the different sea ice types (classified) and the open water within the L-band scenes. The link between the sea ice types and theoretical sea ice freeboards in given in Table V, together with observed sea ice freeboards from the laser scanner. The latter was extracted for the different sea ice types using ROIs. It is observed that the selected sections of classified images (i.e., classified ice types) show good agreement with observed ALS freeboards, and in accordance with the WMO standard for sea ice types [50]. As can be observed in Fig. 13, the standard deviation for the σ_{HH} values within these ROIs are lower for the SFYI (1.67 dB) and RFYMYI (2.31 dB) than for the OW (3.19 dB) and the YI (3.34 dB).

We also report here that similar kind of observations are made for the ALS and SAR acquisitions on April 19, 2015. Figs. 14 and 15 show the drift corrected ALS data set overlaid on ALOS-2 and RS-2 scenes acquired on April 23 along with classification results. Unfortunately, there was no ALS overlap with the TS-X acquisition on that day. We choose these particular sections of the scenes as those sections represent all sea ice classes, i.e., OW, YI, SFYI, and RFYMYI,

TABLE V

ESTIMATED SEA ICE FREEBOARDS FOR THE DIFFERENT SEA ICE TYPES AS WELL AS OBSERVED ALS SEA ICE FREEBOARD. THE SEA ICE THICKNESS IS GIVEN ACCORDING TO [50]

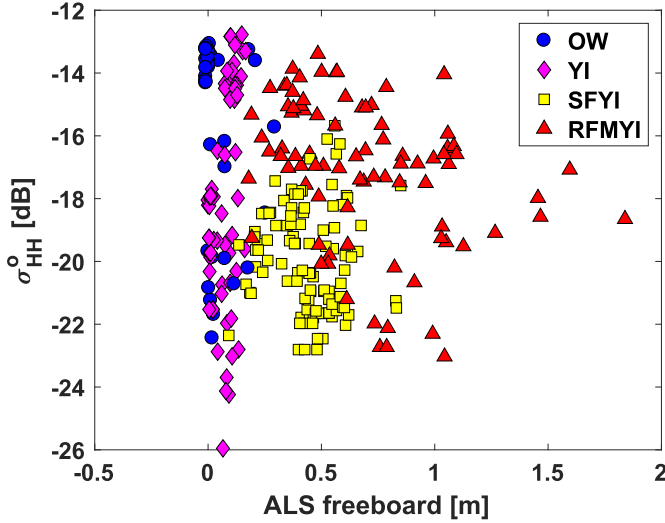| Sea Ice Type	Sea Ice Thickness	Estimated Sea Ice Freeboard	Observed ALS Freeboard
OW	<0.1 m	<0.05 m	0.05 m±0.08 m
YI	0.1 m-0.3 m	0.05 m-0.15 m	0.08 m±0.06 m
SFYI	0.3 m-2.0 m	0.07 m-0.45 m	0.45 m±0.15 m
RFYMYI	> 2 m	>0.36 m	0.71 m±0.34 m

Fig. 13. Comparison of L-band radar backscatter (σ_{HH}) and ALS freeboard measurement over open water (blue circles), YI (purple diamonds), SFYI (yellow squares), and RFYMYI (red triangles) on April 23, 2015.

which have overlapping ALS acquisition. Transects of OW, YI, SFYI, and RFYMYI ice regions are indicated with blue, purple, yellow, and red lines, respectively, in Figs. 14 and 15. These transects are used in Fig. 16, where the ALS-derived freeboard is presented with the overlapping L- and C-band σ_{XX} ($XX = HH, HV, VH$, and VV) over four different ice classes. Similar to the observations from the ROIs we observe that for the OW transect, the ALS-derived freeboard has the value of $\simeq$ 0.0 m, and this is to be expected as open water areas were used as a baseline for freeboard calculations. Note that in this case, the OW part was very narrow and only represented in the middle of Fig. 16(a) indicated by white background. The purple lines in Figs. 14 and 15 represent a prominent portion of YI, which was correctly characterized by the proposed classifier and matches with the ALS measurement [$\simeq$ 0.05–0.1 m, see Fig. 16(b) and Table V]. In the case of SFYI (indicated by yellow lines) and RFYMYI (indicated by red lines), an agreement is observed between L- and C-band σ_{XX}, ALS freeboard, and the classified images. Over the SFYI, the ALS freeboard was estimated to be between 0.2 to 0.8 m and 0.4 to 1.5 m in the case of RFYMYI which is in line with expected freeboard values for these kinds of sea ice types (see Table V). Note that the sigma nought values alone cannot distinguish between the four ice classes.

V. DISCUSSION

In this paper, we presented a sea ice classification methodology developed for X-, C-, and L-band quad-polarimetric SAR imagery, which is capable of generating results within the near real-time requirement of maritime safety and security applications. Colocated observations at the three frequencies were acquired within 7.5 and 7 h for the two different days, respectively. This allows us to directly compare our classification results, as changes in geophysical characteristics of the sea ice can be ignored. In addition, with the help of near-coincident extensive airborne observations, i.e., ALS together with high-resolution photography, we validate our results in the larger spatial extent.

During the feature redundancy and relevancy analysis, we observed that γ (copolarization power ratio) and δ (scattering diversity) play a major role in discriminating OW from thicker ice types, i.e., SFYI and RFYMYI for the L-band and that γ is important at the C-band. The importance of the γ values can also be observed in Fig. 16(b), where for the L-band σ_{HH} and σ_{VV} have a mean difference of 1.57 ± 0.41 dB. From the ROIs, we find that the areas classified as YI have a difference of 1.38 ± 0.78 dB between the σ_{HH} and σ_{VV} channels. The γ parameter was observed to be useful in separating the YI from the surrounding thicker sea ice within the neural network and this has also been observed in many earlier studies, to mention a few [19], [20], [42], [51]–[55]. The surface scattering fraction [τ, see (23)] seems to be very useful for discriminating YI from SFYI. Therefore, we consider that γ and τ are indispensable for the proposed classifier along with δ when one wants to avoid computationally expensive Pauli features.

The importance of the γ parameter for the discrimination of the YI class can also be observed in the transect in Fig. 16(b), where the separation between the σ_{VV} and σ_{HH} values is clearly visible in the L-band data, and it is also present for the C-band data. Within our validation step, we compare the ALS freeboard data for each sea ice class to the polarimetric parameters; though for simplicity in Fig. 16, we only use the σ_{XX} values to illustrate the relationship between the ALS freeboard measurements and the polarimetric SAR-images. We note that the estimated and observed freeboard heights for the respective sea ice classes, as seen in Table V, show good agreement. Furthermore, the YI class has a standard deviation (std) from the mean values for the HH-channel of 2.21 dB. This is higher than the values observed for OW 0.93 dB, SFYI 1.08 dB, and RFYMYI 1.80 dB.

A wide range of backscatter values for YI has also been observed in [52]. Since YI can be made up of newly formed sea ice with varying types of structures such as small-scale ridging and rafting that occur if the ice is subject to wave interaction after being formed during calm stable conditions, this range of values is not surprising. Using photographs combined with sea ice (plus snow) thickness measurements, [24] observed small-scale ridging and rafting within all the open lead areas within the same ALOS-2 and RS-2 scenes that have been used here. Moreover, the RFYMYI has the second highest std value of the four classes. The large variations
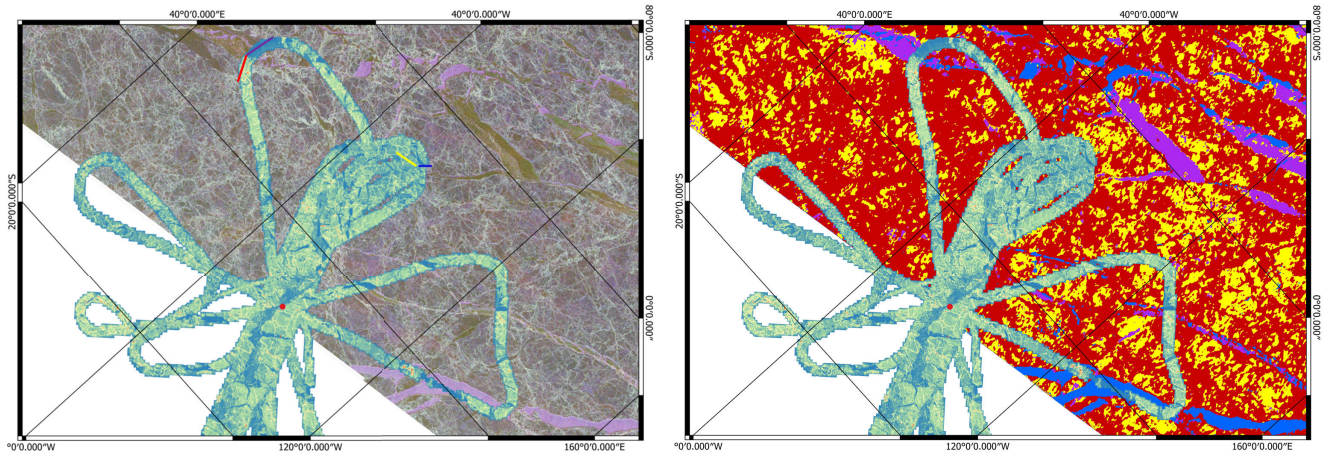
Fig. 14. (Left) ALS freeboard measurement overlaid on geocoded Pauli RGB composite (red: HH-VV, green: HV + VH, and blue: HH + VV) of the ALOS-2 acquisition on April 23, 2015. (Right) Ice classification on ALOS-2 acquisition. Blue: open water/nilas (OW). Purple: YI. Yellow: SFYI. Red: RFYMYI. ALS freeboard color scale according to Fig. 4.
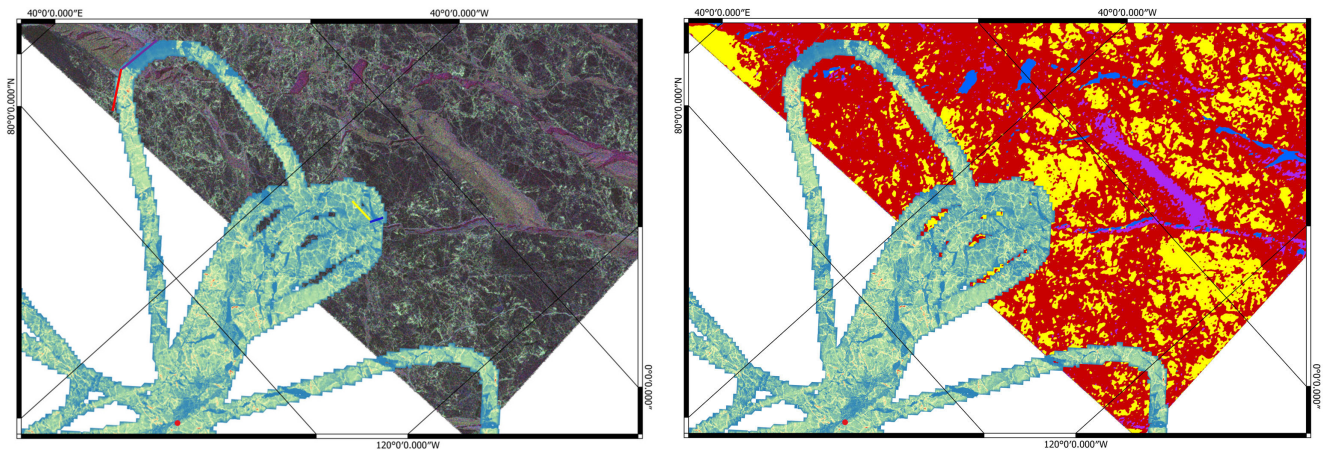

Fig. 15. (Left) ALS freeboard measurement overlaid on geocoded Pauli RGB composite (red: HH-VV, green: HV + VH, and blue: HH + VV) of the RS-2 acquisition on April 23, 2015. (Right) Ice classification on RS-2 acquisition. Blue: open water/nilas (OW). Purple: YI. Yellow: SFYI. Red: RFYMYI. ALS freeboard color scale according to Fig. 4.

in the σ_{XX} values for the YI and RFYMYI classes can be clearly seen in Fig. 16. These significant variations in the σ_{XX} values within certain sea ice type classes are also one of the reasons why backscatter intensity values alone cannot be employed to accurately separate YI from surrounding thicker sea ice. From the ALS freeboard measurements, we observe that the largest variation is found in the RFYMYI class with an std value of 0.34 m. For OW, the standard deviation value was 0.08 m, for YI 0.06 m, and for SFMYI 0.15 m. The widespread for the RFYMYI is likely a consequence of the rougher surface topography observed within the deformed sea ice areas. In Fig. 13, the RFYMYI can also be seen to represent all the ALS freeboard data greater than 1 m and largely contain the σ_{HH} values above −16 dB in Fig. 13, indicative of increased surface backscatter often corresponding to deformed sea ice. The ALS freeboard data combined with the backscatter intensity values, therefore, seem to validate the automatically classified sea ice classes. The combination of the γ values importance for the YI class, clearly observed

in Figs. 7 and 16, with the importance of other computationally inexpensive polarimetric parameters, such as τ and δ, indicates that polarimetric information can improve automatic sea ice classifications.

When it comes to automatic classification and near-real-time product delivery, the overall processing time is crucial. Therefore, the identification of redundant polarimetric features is of the utmost importance. For the C- and X-bands, we found that the Pauli-based features are rather mediocre in terms of feature ranking and can be replaced by other lexicographic features, such as δ and τ. However, for the L-band, we observed that some Pauli-based features, in particular, $H^{(q/d)}$ and $A^{(q/d)}$, play an important role in sea ice type discrimination. The alpha angle [$\alpha^{(q)}$ or $\alpha^{(d)}$] performed inadequately in all frequency bands. Another striking difference between the L-band and the C-/X-band is the performance of geometric intensity [μ, see (24)]; in the case of C/X-band, μ was observed to be one of the best performing polarimetric features. However, in the case of L-band, its performance was rather low. On the
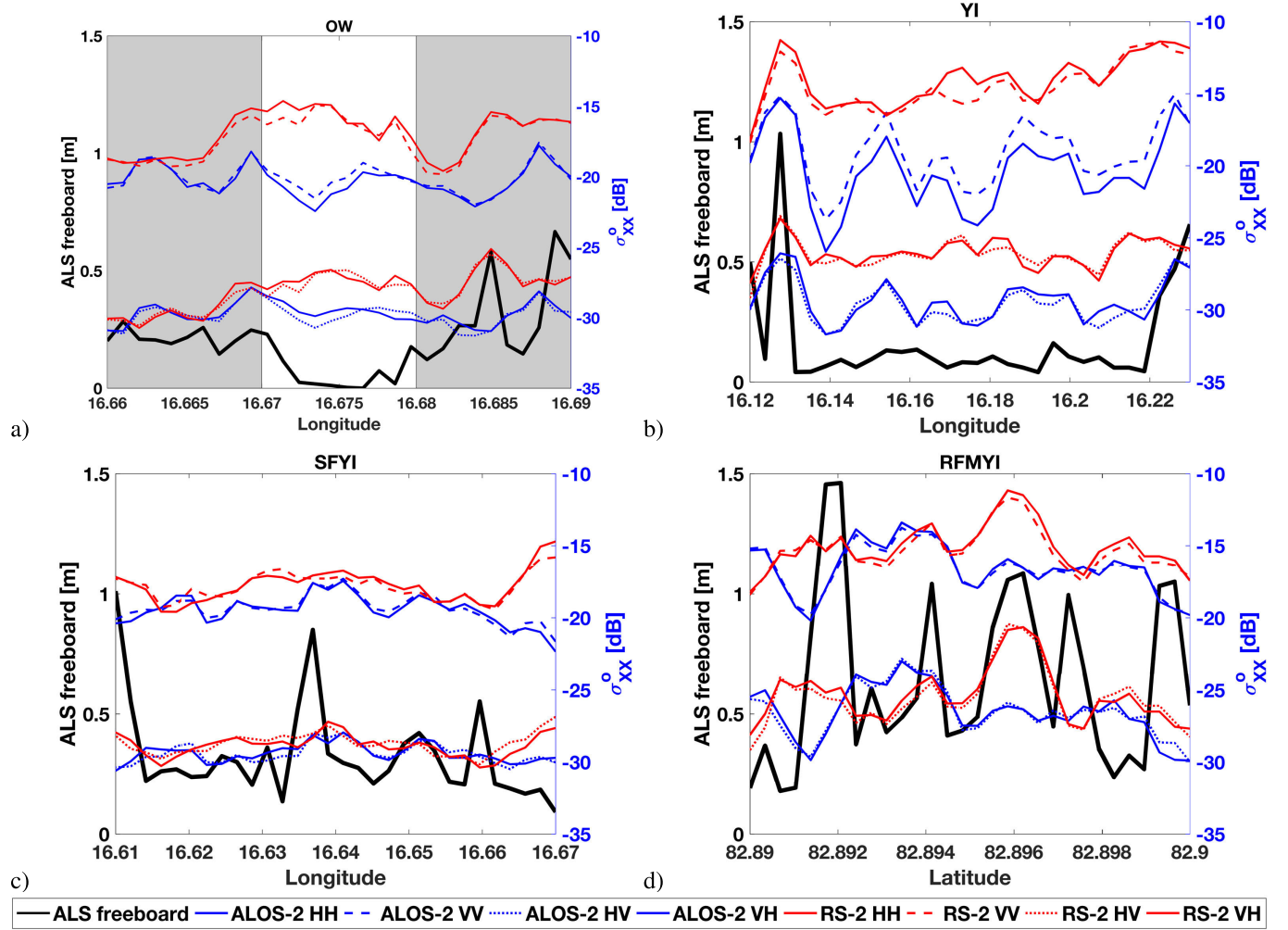
Fig. 16.   Comparison of C- and L-band radar backscatter (σ_{HH}, σ_{HV}, σ_{VH}, and σ_{VV}) and ALS freeboard measurement over (a) open water, (b) YI, (c) SFYI, and (d) RFYMYI on April 23, 2015. Open water (blue), YI (magenta), SFYI (yellow), and RFYMYI (red) transects are indicated in Figs. 14 and 15.

other hand, contrary to the C- and X-bands, the correlation coefficient [ε, see (19)] is extremely useful for the L-band in discriminating YI from SFYI. Polarimetric feature span [span$^{(q)}$ or span$^{(d)}$] seems to provide useful information in all frequency bands. Based on these observations, we observe that the behavior of some polarimetric features in the L-band is different to those obtained from the C- and X-bands. For an near real time automatic classifier, it is, therefore, important to specify which parameters should be used for the different frequencies to achieve the best outcome. Another point, which is important to mention here, is that quad-polarimetry does not necessarily improve the sea ice characterization significantly, and a comparable level of accuracy can be achieved using only the copolarized (HH-VV) channels [18], [29]. Moreover, some of the polarimetric parameters used here, e.g., γ, have directly related compact-polarimetric parameters [56]–[58] and such findings from this paper can be directly transferable to the higher spatial coverage of the compact-polarimetric images. Ongoing and upcoming compact-polarimetric missions include C-band missions, such as RISAT-1 and the Radarsat Constellation Mission, and L-band missions, such as ALOS-2 and ALOS-4.

VI. CONCLUSION

In this paper, we conducted a quantitative comparison of spatially and temporally near coincident quad-polarimetric images in the L-, C-, and X-bands in terms of polarimetric feature evaluation for sea ice classification and validation using airborne data sets. Given the spatial and time correlation of spaceborne and airborne measurements, we can preclude in our findings any impact of sea ice variability. In order to judge in a rigorous and quantitative way the suitability of different polarimetric features, we performed a mutual information-based analysis of the data from all four acquisitions. Based on this, we arrived at the conclusion that, for our purposes, features involving eigendecomposition of the scatter coherency matrix T_3 do not provide informational benefit in the case of C- and X-band data sets. In the case of L-band data set, features derived from coherency matrix T_3 are observed to be useful. In general, the X- and L-bands provide a better discrimination between YI and SFYI/RFYMYI compared with the C-band. The findings about the relevance and redundancy of particular features turned out to be similar for C- and X-bands and slightly different in the case of the L-band. Comparisons

between the ALS-derived sea ice freeboard height and the backscatter intensity values for the derived sea ice classes show that our results are promising in terms of providing inputs for the creation of operational ice charts in the future. However, there are still some limitations related to the use of proposed automatic classification algorithms for ice charting and operational purposes, which are mainly related to incidence angle and seasonal variability along with the limited swaths for fully polarimetric acquisitions. Nevertheless, polarimetric SAR-based automated sea ice classification methodology has the potential to be exploited in operational services with the advent of future, next generation SAR sensors with wide swath compact (hybrid) polarimetric modes.

APPENDIX

POLARIMETRIC FEATURES

The complex backscatter return is denoted by S_{XY}, i.e.,

$$S_{XY} = \sigma_{XY} \exp(i\phi_{XY}) \tag{4}$$

where σ_{XY} denotes the absolute of S_{XY} and ϕ_{XY} denotes the phase angle of S_{XY}, with $X, Y \in \{H, V\}$.

The brackets $\langle \cdot \rangle$ symbolize the local averaging process during polarimetric feature extraction. (The spatial averaging window size was chosen to be 11 pixels for our sample data set throughout this publication.) The scattering vector is commonly analyzed with respect to the lexicographic basis and the Pauli basis. The resulting scattering matrices (averaged covariances) are the well-known covariance matrix S_3 and coherency matrix T_3 (5) and (6), as shown at the bottom of this page,

The dual-polarimetric versions were then defined as

$$S_2 = \begin{pmatrix} S_3(1, 1) & S_3(1, 2) \\ S_3(2, 1) & S_3(2, 2) \end{pmatrix} \tag{7}$$

and

$$T_2 = \begin{pmatrix} T_3(1, 1) & T_3(1, 2) \\ T_3(2, 1) & T_3(2, 2) \end{pmatrix}. \tag{8}$$

The particular features were inspired by the ones outlined in [59]–[61].

The (quad-polarimetric) eigenvalues $\lambda_1^{(q)}$, $\lambda_2^{(q)}$, and $\lambda_3^{(q)}$ of T_3 and the (dual-polarimetric) eigenvalues $\lambda_1^{(d)}$ and $\lambda_2^{(d)}$ of T_2 were used to compute $p_j^{(q)} = \lambda_j^{(q)}/(\lambda_1^{(q)} + \lambda_2^{(q)} + \lambda_3^{(q)})$ and $p_j^{(d)} = \lambda_j^{(d)}/(\lambda_1^{(d)} + \lambda_2^{(d)})$. This was the input for deriving entropy

$$H^{(q)} = -\left(p_1^{(q)} \log_3 \left(p_1^{(q)} \right) + p_2^{(q)} \log_3 \left(p_2^{(q)} \right) + p_3^{(q)} \log_3 \left(p_3^{(q)} \right) \right) \tag{9}$$

and

$$H^{(d)} = -\left(p_1^{(d)} \log_2 \left(p_1^{(d)} \right) + p_2^{(d)} \log_2 \left(p_2^{(d)} \right) \right) \tag{10}$$

and anisotropy

$$A^{(q)} = \frac{\left(p_2^{(q)} - p_3^{(q)} \right)}{\left(p_2^{(q)} + p_3^{(q)} \right)} \tag{11}$$

and

$$A^{(d)} = \frac{\left(p_1^{(d)} - p_2^{(d)} \right)}{\left(p_1^{(d)} + p_2^{(d)} \right)}. \tag{12}$$

From the eigenvectors $v_1^{(q)}$, $v_2^{(q)}$, and $v_3^{(q)}$ of T_3, one obtains

$$\alpha_i^{(q)} = \arccos(v_j^{(q)}(1)), \ j = 1, 2. \tag{13}$$

For comparison, we also computed from the T_2 matrix the $\alpha^{(d)}$ angles [defined analogously with eigenvectors $v_j^{(d)}$ of T_2 instead of $v_j^{(q)}$], simply for the sake of comparison of quad-polarimetric and dual-polarimetric data. The average α angle we defined by

$$\alpha^{(q)} = \alpha_1^{(q)} p_1^{(q)} + \alpha_2^{(q)} p_2^{(q)} + \alpha_3^{(q)} p_3^{(q)} \tag{14}$$

and analogously for the dual-polarimetric case

$$\alpha^{(d)} = \alpha_1^{(d)} p_1^{(d)} + \alpha_2^{(d)} p_2^{(d)} \tag{15}$$

where the classical $H^{(q)}/A^{(q)}/\alpha^{(q)}$ features [59] in the fully polarimetric case have a well-established physical interpretation (e.g., about predominant scattering mechanisms), and such interpretation cannot be expected to hold for our dual-polarimetric adaptions $H^{(d)}/A^{(d)}/\alpha^{(d)}$. Nonetheless, the dual-polarimetric Pauli-based features bear statistical information (possibly without physical meaning) that can characterize different types of sea ice surfaces.

From S_2 and S_3, we derived a number of features, inspired in [60] and [61], as follows.

1) *Copolarization Power Ratio:*

$$\gamma = \frac{\langle |S_{HH}|^2 \rangle}{\langle |S_{VV}|^2 \rangle}. \tag{16}$$

2) *Copol Phase Difference:*

$$\Delta\phi = \phi_{HH} - \phi_{VV}. \tag{17}$$

3) *Real Part of the Copolarization Cross Product:*

$$\rho = |\Re\langle S_{HH} S_{VV}^* \rangle|. \tag{18}$$

4) *Correlation:*

$$\varepsilon = \frac{\langle S_{HH} S_{VV}^* \rangle}{\sqrt{\langle |S_{HH}|^2 \rangle \langle |S_{VV}|^2 \rangle}}. \tag{19}$$

$$S_3 = \begin{pmatrix} \langle |S_{HH}|^2 \rangle & \langle (S_{HH})(S_{VV})^* \rangle & \langle (S_{HH})(S_{HV})^* \rangle \\ \langle (S_{HH})^*(S_{VV}) \rangle & \langle |S_{VV}|^2 \rangle & \langle (S_{VV})(S_{HV})^* \rangle \\ \langle (S_{HH})^*(S_{HV}) \rangle & \langle (S_{VV})^*(S_{HV}) \rangle & \langle |S_{HV}|^2 \rangle \end{pmatrix} \tag{5}$$

$$T_3 = \frac{1}{\sqrt{2}} \begin{pmatrix} \langle |S_{HH} + S_{VV}|^2 \rangle & \langle (S_{HH} + S_{VV})(S_{HH} - S_{VV})^* \rangle & \langle (S_{HH} + S_{VV})(2\ S_{HV})^* \rangle \\ \langle (S_{HH} + S_{VV})^*(S_{HH} - S_{VV}) \rangle & \langle |S_{HH} - S_{VV}|^2 \rangle & \langle (S_{HH} - S_{VV})(2\ S_{HV})^* \rangle \\ \langle (S_{HH} + S_{VV})^*(2\ S_{HV}) \rangle & \langle (S_{HH} - S_{VV})^*(2\ S_{HV}) \rangle & \langle |2(S_{HV})|^2 \rangle \end{pmatrix}. \tag{6}$$

5) *Span of T_2 and T_3:*

$$\text{span}^{(d)} = \text{trace}(T_2) \tag{20}$$

and

$$\text{span}^{(q)} = \text{trace}(T_3). \tag{21}$$

6) *Scattering Diversity (Where $\|\cdot\|_F$ Denotes the Matrix Frobenius Norm):*

$$\delta = \frac{3}{2} \left(1 - \left(\frac{\|T_3\|_F}{\text{span}^{(q)}} \right)^2 \right). \tag{22}$$

7) *Surface Scattering Fraction:*

$$\tau = \frac{\langle |S_{HH} + S_{VV}|^2 \rangle}{\text{span}}. \tag{23}$$

8) *Geometric Intensity μ:*

$$\mu = (\det(T_3))^{(1/3)}. \tag{24}$$

ACKNOWLEDGMENT

REFERENCES

[1] W. Dierking and T. Busche, "Sea ice monitoring by L-band SAR: An assessment based on literature and comparisons of JERS-1 and ERS-1 imagery," *IEEE Trans. Geosci. Remote Sens.*, vol. 44, no. 4, pp. 957–970, Apr. 2006.

[2] M. Arkett, D. Flett, R. D. Abreu, P. Clemente-Colon, J. Woods, and B. Melchior, "Evaluating ALOS-PALSAR for ice monitoring—What can L-band do for the North American ice service?" in *Proc. IEEE Int. Geosci. Remote Sens. Symp. (IGARSS)*, vol. 5. Jul. 2008, pp. V-188–V-191.

[3] J. A. Casey, S. E. Howell, A. Tivy, and C. Haas, "Separability of sea ice types from wide swath C- and L-band synthetic aperture radar imagery acquired during the melt season," *Remote Sens. Environ.*, vol. 174, pp. 314–328, Mar. 2016. [Online]. Available: http://www.sciencedirect.com/science/article/pii/S003442571530242X

[4] D. Flett, R. de Abreu, M. Arkett, and M.-F. Gauthier, "Initial evaluation of Radarsat-2 for operational sea ice monitoring," in *Proc. IEEE Int. Geosci. Remote Sens. Symp. (IGARSS)*, vol. 1. Jul. 2008, pp. I-9–I-12.

[5] N. Zakhvatkina, A. Korosov, S. Muckenhuber, S. Sandven, and M. Babiker, "Operational algorithm for ice–water classification on dual-polarized RADARSAT-2 images," *Cryosphere*, vol. 11, pp. 33–46, Jan. 2017. [Online]. Available: http://www.the-cryosphere.net/11/33/2017/

[6] J. Karvonen, "Operational SAR-based sea ice drift monitoring over the Baltic Sea," *Ocean Sci.*, vol. 8, no. 4, pp. 473–483, 2012.

[7] J. Karvonen, J. Vainio, M. Marnela, P. Eriksson, and T. Niskanen, "A comparison between high-resolution EO-based and ice analyst-assigned sea ice concentrations," *IEEE J. Sel. Topics Appl. Earth Observ. Remote Sens.*, vol. 8, no. 4, pp. 1799–1807, Apr. 2015.

[8] W. Dierking and C. Wesche, "C-band radar polarimetry—Useful for detection of icebergs in sea ice?" *IEEE Trans. Geosci. Remote Sens.*, vol. 52, no. 1, pp. 25–37, Jan. 2014.

[9] A. Frost, R. Ressel, and S. Lehner, "Automated iceberg detection using high-resolution X-band SAR images," *Can. J. Remote Sens.*, vol. 42, no. 4, pp. 354–366, 2016.

[10] D. A. Clausi and B. Yue, "Comparing cooccurrence probabilities and Markov random fields for texture analysis of SAR sea ice imagery," *IEEE Trans. Geosci. Remote Sens.*, vol. 42, no. 1, pp. 215–228, Jan. 2004.

[11] S. Ochilov and D. A. Clausi, "Operational SAR sea-ice image classification," *IEEE Trans. Geosci. Remote Sens.*, vol. 50, no. 11, pp. 4397–4408, Nov. 2012.

[12] N. Y. Zakhvatkina, V. Y. Alexandrov, O. M. Johannessen, S. Sandven, and I. Y. Frolov, "Classification of sea ice types in ENVISAT synthetic aperture radar images," *IEEE Trans. Geosci. Remote Sens.*, vol. 51, no. 5, pp. 2587–2600, May 2013.

[13] W. Dierking and L. T. Pedersen, "Monitoring sea ice using envisat ASAR—A new era starting 10 years ago," in *Proc. IEEE Int. Geosci. Remote Sens. Symp.*, Jul. 2012, pp. 1852–1855.

[14] R. Ressel, A. Frost, and S. Lehner, "A neural network-based classification for sea ice types on X-band SAR images," *IEEE J. Sel. Topics Appl. Earth Observ. Remote Sens.*, vol. 8, no. 7, pp. 3672–3680, Jul. 2015.

[15] S. Leigh, Z. Wang, and D. Clausi, "Automated Ice-Water Classification Using Dual Polarization SAR Satellite Imagery," *IEEE Trans. Geosci. Remote Sens.*, vol. 52, no. 9, pp. 5529–5539, Sep. 2014.

[16] R. Kwok, E. Rignot, B. Holt, and R. Onstott, "Identification of sea ice types in spaceborne synthetic aperture radar data," *J. Geophys. Res., Oceans*, vol. 97, no. C2, pp. 2391–2402, 1992. [Online]. Available: http://dx.doi.org/10.1029/91JC02652

[17] J. Karvonen, M. Similä, and M. Makynen, "Open water detection from Baltic Sea ice Radarsat-1 SAR imagery," *IEEE Geosci. Remote Sens. Lett.*, vol. 2, no. 3, pp. 275–279, Jul. 2005.

[18] E. Rignot and M. R. Drinkwater, "Winter sea-ice mapping from multi-parameter synthetic-aperture radar data," *J. Glaciol.*, vol. 40, no. 134, pp. 31–45, 1994.

[19] M. R. Drinkwater, R. Kwok, D. P. Winebrenner, and E. Rignot, "Multi-frequency polarimetric synthetic aperture radar observations of sea ice," *J. Geophys. Res., Oceans*, vol. 96, no. C11, pp. 20679–20698, 1991. [Online]. Available: http://dx.doi.org/10.1029/91JC01915

[20] H. Wakabayashi, T. Matsuoka, K. Nakamura, and F. Nishio, "Polarimetric Characteristics of sea ice in the sea of Okhotsk observed by airborne L-band SAR," *IEEE Trans. Geosci. Remote Sens.*, vol. 42, no. 11, pp. 2412–2425, Nov. 2004.

[21] J. S. Lee, M. R. Grunes, and R. Kwok, "Classification of multi-look polarimetric SAR imagery based on complex Wishart distribution," *Int. J. Remote Sens.*, vol. 15, no. 11, pp. 2299–2311, Jul. 1994. [Online]. Available: http://dx.doi.org/10.1080/01431169408954244

[22] M.-A. N. Moen *et al.*, "Comparison of feature based segmentation of full polarimetric SAR satellite sea ice images with manually drawn ice charts," *Cryosphere*, vol. 7, no. 6, pp. 1693–1705, 2013. [Online]. Available: http://www.the-cryosphere.net/7/1693/2013

[23] M.-A. N. Moen, S. N. Anfinsen, A. P. Doulgeris, A. H. H. Renner, and S. Gerland, "Assessing polarimetric SAR sea-ice classifications using consecutive day images," *Ann. Glaciol.*, vol. 56, no. 69, pp. 285–294, 2015.

[24] A. M. Johansson *et al.*, "Combined observations of Arctic sea ice with near-coincident colocated X-band, C-band, and L-band SAR satellite remote sensing and helicopter-borne measurements," *J. Geophys. Res., Oceans*, vol. 122, no. 1, pp. 669–691, 2017. [Online]. Available: http://dx.doi.org/10.1002/2016JC012273

[25] R. Ressel and S. Singha, "Comparing near coincident space borne C and X band fully polarimetric SAR data for Arctic sea ice classification," *Remote Sens.*, vol. 8, no. 3, p. 198, 2016. [Online]. Available: http://www.mdpi.com/2072-4292/8/3/198

[26] H. Peng, F. Long, and C. Ding, "Feature selection based on mutual information criteria of max-dependency, max-relevance, and min-redundancy," *IEEE Trans. Pattern Anal. Mach. Intell.*, vol. 27, no. 8, pp. 1226–1238, Aug. 2005.

[27] S. Nissen, "Neural networks made simple," Dept. Comput. Sci. Univ. Copnhagen, Copnhagen, Denmark, Tech. Rep. 2, 2005.

[28] A. V. Bogdanov, S. Sandven, O. M. Johannessen, V. Y. Alexandrov, and L. P. Bobylev, "Multisensor approach to automated classification of sea ice image data," *IEEE Trans. Geosci. Remote Sens.*, vol. 43, no. 7, pp. 1648–1664, Jul. 2005.

[29] R. Ressel, S. Singha, S. Lehner, A. Rösel, and G. Spreen, "Investigation into different polarimetric features for sea ice classification using X-band synthetic aperture radar," *IEEE J. Sel. Topics Appl. Earth Observ. Remote Sens.*, vol. 9, no. 7, pp. 3131–3143, Jul. 2016.

[30] (2014). *Ice Chart Colour Code Standard: Wmo/td-no. 1215*. [Online]. Available: http://www.jcomm.info/index.php?option=com_oe&task=viewDocumentRecord&docID=4914

[31] M. A. Granskog, P. Assmy, S. Gerland, G. Spreen, H. Steen, and L. H. Smedsrud, "Arctic research on thin ice: Consequences of arctic sea ice loss," *EOS*, vol. 97, Jan. 2016. [Online]. Available: https://eos.org/project-updates/arctic-research-on-thin-ice-consequences-of-arctic-sea-ice-loss

[32] A. Rösel *et al.* (2016). *N-ICE2015 Total (Snow and Ice) Thickness Data From EM31 V1*. [Online]. Available: https://doi.org/10.21334/npolar.2016.70352512

[33] A. Rösel *et al.* (2016). *N-ICE2015 Snow Depth Data With Magnaprobe V1*. [Online]. Available: https://doi.org/10.21334/npolar.2016.3d72756d

[34] M. A. Granskog *et al.*, "Snow contribution to first-year and second-year arctic sea ice mass balance north of svalbard," *J. Geophys. Res., Oceans*, vol. 122, no. 3, pp. 2539–2549, 2017. [Online]. Available: http://dx.doi.org/10.1002/2016JC012398

[35] S. R. Hudson, L. Cohen, and V. Walden. (2015). *N-ICE2015 Surface Meteorology V1*. [Online]. Available: https://doi.org/10.21334/npolar.2015.056a61d1

[36] L. Cohen, S. R. Hudson, V. P. Walden, R. M. Graham, and M. A. Granskog, "Meteorological conditions in a thinner Arctic sea ice regime from winter to summer during the Norwegian Young Sea Ice expedition (N-ICE2015)," *J. Geophys. Res., Atmos.*, vol. 122, no. 14, pp. 7235–7259, 2017.

[37] P. Itkin *et al.*, "Thin ice and storms: Sea ice deformation from buoy arrays deployed during N-ICE2015," *J. Geophys. Res., Oceans*, vol. 122, no. 6, pp. 4661–4674, 2017. [Online]. Available: http://dx.doi.org/10.1002/2016JC012403

[38] S. M. Hvidegaard, H. Skourup, J. Wilkinson, R. Ladkin, and R. Forsberg, "Data collection and processing report- for ICE-ARC airborne campaign 2015," Nat. Space Inst., Techn. Univ. Denmark, Kongens Lyngby, Denmark, Tech. Rep. ICE-ARC-021, 2016.

[39] P. Itkin, G. Spreen, S. M. Hvidegaard, H. Skourup, J. Wilkinson, S. Gerland and M. A. Granskog, "Contribution of sea ice deformation to sea ice mass balance: A case study from an N-ICE2015 storm," *Geophys. Res. Lett.*, vol. 45, no. 2, pp. 789–796, 2017.

[40] S. M. Hvidegaard and R. Forsberg, "Sea-ice thickness from airborne laser altimetry over the arctic ocean north of greenland," *Geophys. Res. Lett.*, vol. 29, no. 20, pp. 13-1–13-4, 2002, 1952. [Online]. Available: http://dx.doi.org/10.1029/2001GL014474

[41] W. Dierking, H. Skriver, and P. Gudmandsen, "On the improvement of sea ice classification by means of radar polarimetry," in *Proc. 23rd EARSeL Symp., Remote Sens. Transition*, 2004, pp. 203–209.

[42] T. Geldsetzer and J. J. Yackel, "Sea ice type and open water discrimination using dual co-polarized C-band SAR," *Can. J. Remote Sens.*, vol. 35, no. 1, pp. 73–84, 2009. [Online]. Available: http://dx.doi.org/10.5589/m08-075

[43] C. Brekke, B. Holt, C. Jones, and S. Skrunes, "Discrimination of oil spills from newly formed sea ice by synthetic aperture radar," *Remote Sens. Environ.*, vol. 145, pp. 1–14, Apr. 2014. [Online]. Available: http://www.sciencedirect.com/science/article/pii/S0034425714000285

[44] A. M. Johansson, C. Brekke, G. Spreen, and J. A. King, "X-, C-, and L-band SAR signatures of newly formed sea ice in Arctic leads during winter and spring," *Remote Sens. Environ.*, vol. 204, pp. 162–180, Jan. 2018. [Online]. Available: http://www.sciencedirect.com/science/article/pii/S0034425717304960

[45] B. B. Thomsen, S. Nghiem, and R. Kwok, "Polarimetric C-band SAR observations of sea ice in the Greenland Sea," in *Proc. IEEE Int. Geosci. Remote Sens. Symp.*, Jul. 1998, pp. 2502–2504.

[46] L. Yu and H. Liu, "Feature selection for high-dimensional data: A fast correlation-based filter solution," in *Proc. 20th Int. Conf. Mach. Learn. (ICML)*, 2003, pp. 856–863.

[47] J. C. Comiso, P. Wadhams, W. B. Krabill, R. N. Swift, J. P. Crawford, and W. B. Tucker, "Top/bottom multisensor remote sensing of arctic sea ice," *J. Geophys. Res., Oceans*, vol. 96, no. C2, pp. 2693–2709, 1991. [Online]. Available: http://dx.doi.org/10.1029/90JC02466

[48] P. Wadhams, W. B. Tucker, III, W. B. Krabill, R. N. Swift, J. C. Comiso, and N. R. Davis, "Relationship between sea ice freeboard and draft in the arctic basin, and implications for ice thickness monitoring," *J. Geophys. Res., Oceans*, vol. 97, no. C12, pp. 20325–20334, 1992. [Online]. Available: http://dx.doi.org/10.1029/92JC02014

[49] M. J. Doble, H. Skourup, P. Wadhams, and C. A. Geiger, "The relation between arctic sea ice surface elevation and draft: A case study using coincident AUV sonar and airborne scanning laser," *J. Geophys. Res., Oceans*, vol. 116, no. C8, 2011, paper c00E03. [Online]. Available: http://dx.doi.org/10.1029/2011JC007076

[50] *WMO Sea-Ice Nomenclature: Wmo/td-no. 259*. Accessed: Mar. 22, 2017. [Online]. Available: http://www.jcomm.info/index.php?option=com_oe&task=viewDocumentRecord&docID=4438

[51] M. Brath, S. Kern, and D. Stammer, "Sea ice classification during freeze-up conditions with multifrequency scatterometer data," *IEEE Trans. Geosci. Remote Sens.*, vol. 51, no. 6, pp. 3336–3353, Jun. 2013.

[52] W. Dierking, "Mapping of different sea ice regimes using images from sentinel-1 and ALOS synthetic aperture radar," *IEEE Trans. Geosci. Remote Sens.*, vol. 48, no. 3, pp. 1045–1058, Mar. 2010.

[53] K. Nakamura, H. Wakabayashi, K. Naoki, F. Nishio, T. Moriyama, and S. Uratsuka, "Observation of sea-ice thickness in the sea of Okhotsk by using dual-frequency and fully polarimetric airborne SAR (pi-SAR) data," *IEEE Trans. Geosci. Remote Sens.*, vol. 43, no. 11, pp. 2460–2469, Nov. 2005.

[54] X. Zhang, W. Dierking, J. Zhang, J. Meng, and H. Lang, "Retrieval of the thickness of undeformed sea ice from simulated c-band compact polarimetric SAR images," *Cryosphere*, vol. 10, no. 4, pp. 1529–1545, 2016. [Online]. Available: https://www.the-cryosphere.net/10/1529/2016/

[55] R. G. Onstott, *SAR and Scatterometer Signatures of Sea Ice*. Washington, DC, USA: American Geophysical Union, 1992, pp. 73–104. [Online]. Available: http://dx.doi.org/10.1029/GM068p0073

[56] S. R. Cloude, D. G. Goodenough, and H. Chen, "Compact decomposition theory," *IEEE Geosci. Remote Sens. Lett.*, vol. 9, no. 1, pp. 28–32, Jan. 2012.

[57] T. Geldsetzer, M. Arkett, T. Zagon, F. Charbonneau, J. J. Yackel, and R. K. Scharien, "All-season compact-polarimetry C-band SAR observations of sea ice," *Can. J. Remote Sens.*, vol. 41, no. 5, pp. 485–504, 2015. [Online]. Available: http://dx.doi.org/10.1080/07038992.2015.1120661

[58] S. Singha and R. Ressel, "Arctic sea ice characterization using RISAT-1 compact-pol sar imagery and feature evaluation: A case study over northeast greenland," *IEEE J. Sel. Topics Appl. Earth Observ. Remote Sens.*, vol. 10, no. 8, pp. 3504–3514, Aug. 2017.

[59] S. R. Cloude and E. Pottier, "An entropy based classification scheme for land applications of polarimetric SAR," *IEEE Trans. Geosci. Remote Sens.*, vol. 35, no. 1, pp. 68–78, Jan. 1997.

[60] S. Skrunes, C. Brekke, and T. Eltoft, "Characterization of marine surface slicks by radarsat-2 multipolarization features," *IEEE Trans. Geosci. Remote Sens.*, vol. 52, no. 9, pp. 5302–5319, Sep. 2014.

[61] J. Praks, E. C. Koeniguer, and M. T. Hallikainen, "Alternatives to target entropy and alpha angle in SAR polarimetry," *IEEE Trans. Geosci. Remote Sens.*, vol. 47, no. 7, pp. 2262–2274, Jul. 2009.

Suman Singha (M'15) received the M.Tech. degree in remote sensing from IIT Roorkee, Roorkee, India, in 2009, and the M.Sc. degree in remote sensing and the Ph.D. degree in microwave remote sensing from the University of Hull, Hull, U.K., in 2010 and 2014, respectively.

He was a Visiting Scientist with the European Maritime Safety Agency, Lisbon, Portugal, in 2012. Since 2013, he has been with the Remote Sensing Technology Institute, German Aerospace Center, Bremen, Germany, as a Research Scientist. His research interests include the application of artificial intelligence and machine vision approaches to classify traditional and polarimetric synthetic aperture radar images with an emphasis on sea ice classification and oil spill detection.

Malin Johansson (M'17) received the M.Sc. degree in physical oceanography from Gothenburg University, Gothenburg, Sweden, in 2005, and the Ph.D. degree in physical geography remote sensing from Stockholm University, Stockholm, Sweden, in 2012.

She was a Post-Doctoral Researcher with the Radar Remote Sensing Group, Department of Earth and Space Sciences, Chalmers University of Technology, Gothenburg. She is currently a Post-Doctoral Researcher with the University of Tromsø The Arctic University of Norway, Tromsø, Norway. Her research interests include the remote sensing of sea ice and oil spills using spaceborne synthetic aperture radar.

Nicholas Hughes (M'09) received the B.Sc. degree (Hons.) in physical geography from the University of Hull, Hull, U.K., in 1994.

He was a Research Associate with the Scott Polar Research Institute, University of Cambridge, Cambridge, U.K., from 1998 to 2003, and a Research Scientist with the Scottish Association for Marine Science, Oban, U.K., from 2003 to 2007. Since 2007, he has been a Leader of the Norwegian Ice Service, Tromsø, Norway. His research interests include the spaceborne and underwater remote sensing of sea ice and the operational development of geospatial analysis techniques.

Sine Munk Hvidegaard received the Ph.D. degree in geophysics from the University of Copenhagen, Copenhagen, Denmark, in 2005, with a focus on airborne ice altimetry methods for the calibration and validation of Cryosat.

She is currently a Senior Advisor with the National Space Institute (DTU Space), Technical University of Denmark, Kongens Lyngby, Denmark, where she has continued her research on remote sensing of the cryosphere and earth observations from aircrafts and satellite especially for satellite validation purposes.

Henriette Skourup received the M.Sc. degree in geophysics and the Ph.D. degree in satellite remote sensing of Arctic sea ice freeboard heights, gravity anomalies, and dynamic topography from the University of Copenhagen, Copenhagen, Denmark, in 2004 and 2010, respectively.

She has 20 years of experience in the scientific and operational sea ice community. She was a part-time Sea Ice Analyst with the Operational Sea Ice Mapping Division, Danish Meteorological Institute, Copenhagen. Since 2004, she has been with the Geodynamics Department, National Space Institute (DTU Space), Technical University of Denmark, Kongens Lyngby, Denmark, as a Research Scientist. Her research interests include sea ice thickness obtained from satellite altimetry. As a large part of her work includes the validation of satellite altimetry missions, she has coordinated and participated in numerous airborne field campaigns in the Arctic.